AGU PUBLICATIONS

JGR

Journal of Geophysical Research: Solid Earth

RESEARCH ARTICLE
10.1002/2014JB011078

Key Points:
- Forward modeled mantle structure of circum-Arctic region since Jurassic
- Subduction-driven dynamic topography linked to regional subsidence and uplift
- Modeled Panthalassa, Arctic, and Mongol-Okhotsk slabs compared to seismic tomography

Supporting Information:
- Readme
- Text S1 and Tables S1–S3
- Figure S1
- Figure S2
- Figure S3
- Figure S4
- Figure S5
- Figure S6
- Figure S7
- Figure S8
- Figure S9
- Figure S10
- Figure S11
- Figure S12
- Figure S13
- Figure S14
- Figure S15

Correspondence to:
G. E. Shephard,
g.e.shephard@geo.uio.no

Citation:
Shephard, G. E., N. Flament, S. Williams, M. Seton, M. Gurnis, and R. D. Müller (2014), Circum-Arctic mantle structure and long-wavelength topography since the Jurassic, *J. Geophys. Res. Solid Earth*, *119*, 7889–7908, doi:10.1002/2014JB011078.

Received 3 MAR 2014
Accepted 7 SEP 2014
Accepted article online 11 SEP 2014
Published online 6 OCT 2014

Circum-Arctic mantle structure and long-wavelength topography since the Jurassic

G. E. Shephard[1,2], N. Flament[1], S. Williams[1], M. Seton[1], M. Gurnis[3], and R. D. Müller[1]

[1]EarthByte Group, School of Geosciences, University of Sydney, Sydney, New South Wales, Australia, [2]Centre for Earth Evolution and Dynamics, Department of Geosciences, University of Oslo, Oslo, Norway, [3]Seismological Laboratory, California Institute of Technology, Pasadena, California, USA

Abstract The circum-Arctic is one of the most tectonically complex regions of the world, shaped by a history of ocean basin opening and closure since the Early Jurassic. The region is characterized by contemporaneous large-scale Cenozoic exhumation extending from Alaska to the Atlantic, but its driving force is unknown. We show that the mantle flow associated with subducted slabs of the South Anuyi, Mongol-Okhotsk, and Panthalassa oceans have imparted long-wavelength deflection on overriding plates. We identify the Jurassic-Cretaceous South Anuyi slab under present-day Greenland in seismic tomography and numerical mantle flow models. Under North America, we propose the "Farallon" slab results from Andean-style ocean-continent convergence around ~30°N and from a combination of ocean-continent and intraoceanic subduction north of 50°N. We compute circum-Arctic dynamic topography through time from subduction-driven convection models and find that slabs have imparted on average <1–16 m/Myr of dynamic subsidence across the region from at least 170 Ma to ~50 Ma. With the exception of Siberia, the main phase of circum-Arctic dynamic subsidence has been followed either by slowed subsidence or by uplift of <1–6 m/Myr on average to present day. Comparing these results to geological inferences suggest that subduction-driven dynamic topography can account for rapid Middle to Late Jurassic subsidence in the Slave Craton and North Slope (respectively, <15 and 21 m/Myr, between 170 and 130 Ma) and for dynamic subsidence (<7 m/Myr, ~170–50 Ma) followed by dynamic uplift (<6 m/Myr since 50 Ma) of the Barents Sea region. Combining detailed kinematic reconstructions with geodynamic modeling and key geological observations constitutes a powerful tool to investigate the origin of vertical motion in remote regions.

1. Introduction

The long-wavelength surface deformation driven by viscous stresses from mantle flow, *dynamic topography* [e.g., *Hager et al*., 1985; *Gurnis*, 1992; *Flament et al*., 2013], remains poorly investigated across the circum-Arctic. This is despite a long-lived, complex history of subduction since at least the Jurassic, which is expected to have induced deflections of overriding lithosphere. Existing studies of Phanerozoic vertical motions of the circum-Arctic, from the North Atlantic to Alaska (Figure 1), reveal a history of periodic subsidence and uplift and tilted erosion surfaces [e.g., *Stuevold and Eldholm*, 1996; *Japsen and Chalmers*, 2000]. These vertical motions have been attributed to mafic underplating, intraplate stress, plume ascent, and rifting, but these mechanisms cannot account for the contemporaneous and widespread correlation of subsidence and uplift. Furthermore, the potential contribution of subduction-driven mantle flow to topography has generally been overlooked for this area.

In contrast to studies focused on continental interiors [e.g., *Lithgow-Bertelloni and Silver*, 1998; *Pysklywec and Mitrovica*, 1998; *Spasojevic et al*., 2009; *Shephard et al*., 2010; *Flowers et al*., 2012], isolating the component of long-wavelength dynamic topography across the circum-Arctic is inherently complicated by extensive plate boundary changes and multiple tectonic regimes, as well as large uncertainties and poor constraints on oceanic distribution and age and lithospheric thickness and density. To date, there is no published study of time-dependent dynamic topography of the circum-Arctic.

A recently refined plate tectonic reconstruction for the circum-Arctic [*Shephard et al*., 2013] details the opening and closing history of several Mesozoic ocean basins (Figure 2 and Figure S1 in the supporting information). These now-subducted ocean basins comprise the following: (1) parts of Panthalassa (palaeo-Pacific ocean basin) including the Farallon and Izanagi plates and potentially additional microplates

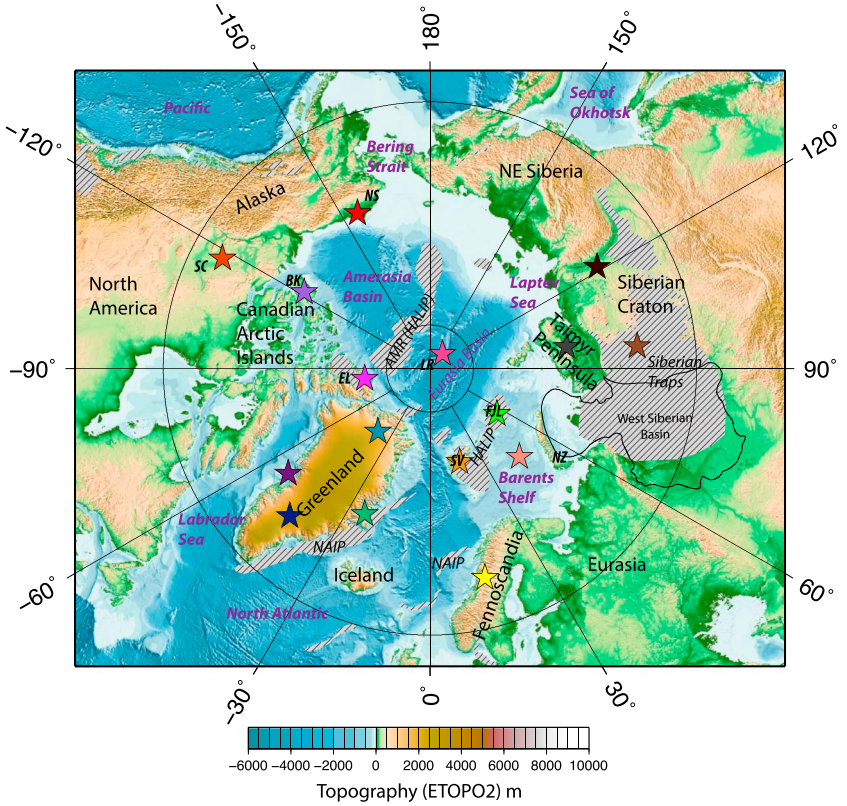

Figure 1. Topography (ETOPO2) and overview of the circum-Arctic with main tectonic and geographic features labeled. AMR, Alpha-Mendeleev Ridge; BK, Banks Island; EL, Ellesmere Island; FJL, Franz Josef Land; LR, Lomonosov Ridge; NS, North Slope; NZ, Novaya Zemlya; SC, Slave Craton; SV, Svalbard. Large Igneous Provinces (LIPs), including the North Atlantic Igneous Province (NAIP), the High Arctic LIP (HALIP), and Siberian Traps, are shown in hatched grey. Outline of West Siberian Basin in black. Colored stars are the present-day locations of selected points for dynamic topography analysis (Figures 6–8).

such as the Cache Creek Ocean, (2) the South Anuyi Ocean (also known as Angayucham Ocean), once located between Siberia and North America, and (3) the Oimyakon Ocean that existed between the Siberian Craton and the rifted blocks of northeast Siberia. Based on a comparison of reconstructed subduction locations (such as in Figures 3–5) and seismic tomography, *Shephard et al.* [2013] interpreted these predominantly Jurassic slabs to be located in the lower mantle beneath the present-day Arctic, from Greenland and the North Atlantic to the East Siberian shelf.

With advances in numerical mantle flow models and plate kinematic reconstructions, the study of long-wavelength subsidence and uplift as a response to the viscous stresses imparted by sinking slabs has gained much attention [e.g., *Husson*, 2006; *Liu et al*., 2008; *Spasojevic et al*., 2009]. A limitation on predictions of mantle heterogeneity as a function of subduction history is the spatiotemporal accuracy of the imposed plate tectonic reconstruction. Thus, using plate reconstructions with a history of subduction consistent with the geological record is essential for reconciling predicted long-wavelength dynamic topography with independent observations from the stratigraphic record. Here we present a time-dependent forward mantle circulation model with surface kinematics derived from the plate reconstruction of *Shephard et al.* [2013] and compare computed dynamic topography across the Arctic to independent observations of nontectonic vertical motion.

2. Methods

We use a workflow that assimilates global surface kinematics, the thermal structure of the lithosphere, and the shallow portion of subducting slabs [*Bower et al*., 2013; *Flament et al*., 2013; D. Bower et al., Assimilating lithosphere and slab history in 4-D dynamic Earth models, *Earth and Planetary Science Letters*,

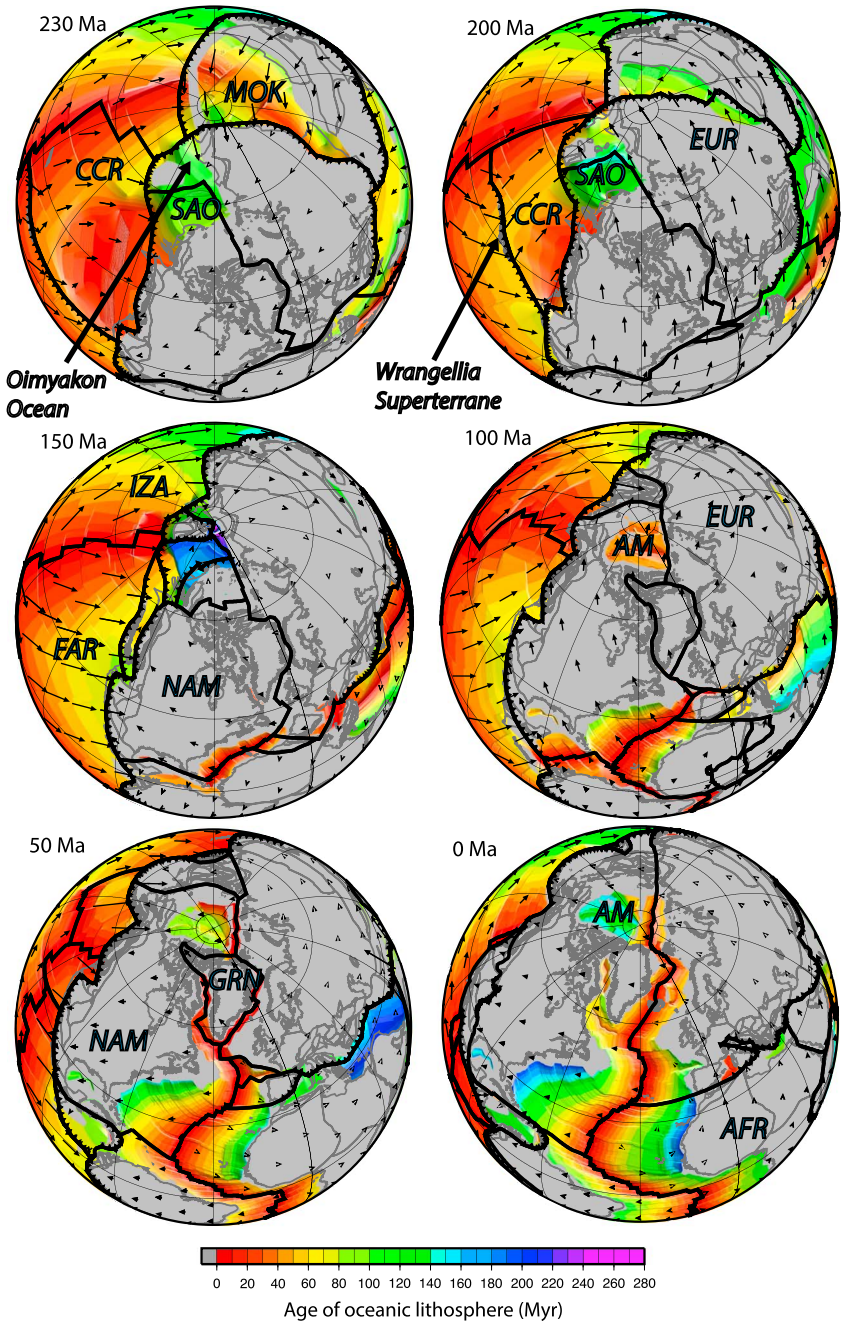

Figure 2. Evolution (230–0 Ma) of the plate reconstruction [*Shephard et al*., 2013] (with a modified reference frame, Table 2) assimilated in the mantle flow models. The absolute reference frame used here is that of case C1. Reconstructed plate boundaries (black lines with teeth located on overriding plate), coastlines (dark grey lines), continental lithosphere (grey polygons), and ages of oceanic lithosphere (see color scale) are shown, as well as velocities (black arrows). Major plates and oceans labeled as AM, Amerasia Basin; AFR, Africa; CCR, Cache Creek oceanic plate; EUR, Eurasia; GRN, Greenland; FAR, Farallon; IZA, Izanagi; MOK, Mongol-Okhostk; NAM, North America; and SAO, South Anuyi Oceans. Orthographic projection centered on 30°W. Additional reconstruction ages are shown in Figure S1.

manuscript in review, 2014] based on global tectonic reconstructions in forward mantle flow models computed using *CitcomS* [e.g., *Zhong et al*., 2000]. This progressive slab assimilation method (Bower et al., in review) ensures that the buoyancy flux is consistent with the plate reconstructions, in contrast to models that only use time-dependent surface kinematic conditions [e.g., *Bunge et al*., 1998]. As a consequence, the

Table 1. Mantle Parameters Used in Numerical Models

Parameter	Value
Reference viscosity	1×10^{21} Pa s
Reference density	4000 kg m^{-3}
Viscosity structure	See Table 2
Thermal expansion coefficient	3×10^{-5} K^{-1}
Gravity acceleration	9.81 m s^{-2}
Temperature change across the mantle (ΔT)	2815 K
Thermal diffusivity	1×10^{-6} m^2 s^{-1}
Surface temperature	273 K
Temperature offset (T_η)	452 K
Activation energy (E_η upper mantle)	100 kJ mol^{-1}
Activation energy (E_η lower mantle)	33 kJ mol^{-1}
Background mantle temperature (T_b)	1680 K
Rayleigh number	7.8×10^8
Core radius	3504 km
Earth radius	6371 km
Average surface resolution	50 × 50 × 15 km
Average core-mantle boundary (CMB) resolution	28 × 28 × 27 km

amplitude of present-day dynamic topography is also more consistent with that of the residual topography for models with progressive data assimilation (Bower et al., in review). We solve the equations for conservation of mass, momentum, and energy using the Boussinesq approximation. We include temperature and pressure-dependent viscosity and thermochemical piles via a 113 km thick, hot, higher-density layer at the base of the mantle (Table 1). The pressure and temperature dependence of viscosity is defined as

$$\eta = \eta_0(r) \exp\left(\frac{E_\eta}{T + T_\eta} - \frac{E_\eta}{T_b + T_\eta}\right) \quad (1)$$

where $\eta_0(r)$ is a prefactor defined for four layers including three subdivisions of the upper mantle (UM): lithosphere above 160 km, asthenosphere 160–310 km, and upper mantle 310–670 km and the lower mantle (LM) below 670 km (see Tables 1 and 2). E_η is the activation energy, dimensionalized according to $E' = E/(R \times \Delta\ (T))$, where E' is the nondimensional activation energy and $R = 8.314$ J mol^{-1} K^{-1}. T_b is the background temperature of the mantle, and T_η is a temperature offset. Lateral viscosity variations are limited to 3 orders of magnitude (between 1.10^{20} Pa s and 1.10^{23} Pa s). Main model parameters are listed in Tables 1 and 2 (see *Flament et al.* [2014] for more details).

Uncertain model parameters, including initial conditions, mantle rheology, reference frame, and density of the basal layer, were tested across multiple cases (Tables 2 and S3 and Figures S14 and S15). This analysis allows us to define a reference case (C1; Figures 2–8, S1, S2, S5, and S9 and Table 2) which is based on the reconstruction of *Shephard et al.* [2013] extended to 230 Ma and with a new absolute reference frame that minimizes the net lithospheric rotation (NLR; see "Supplementary Methods," Table 2, and Figure S13). Maintaining NLR to geodynamically reasonable bounds (<0.26°/Myr) [*Conrad and Behn*, 2010] should minimize offsets in the absolute location of subduction zones through time in coupled plate-mantle models [*Bower et al.*, 2013].

Table 2. Acronyms and Model Details Referred to in This Study

Name/Acronym	Base Plate Reconstruction	Absolute Reference Frame (Prior to NLR Correction)	Net Lithospheric Rotation (NLR) Correction	Viscosity Profile[a] Initial Slab Depth Slab Dip Basal Layer Density
C1	*Shephard et al.* [2013] (also *Zahirovic et al.* [2013] for SE Asia region)	Moving hotspots 0–70 Ma [*Torsvik et al.*, 2008] True Polar Wander (TPW)-corrected palaeomagnetic 105–200 Ma [*Steinberger and Torsvik*, 2008] (interpolation between 70 and 105 Ma)	Minimized from plate reconstruction (NLR <0.4°/Myr, Figure S13) and by using new poles of rotation for E-W Antarctica [*Granot et al.*, 2013][b]	1,1,1,100 1210 km 45° (<425 km) then 90° +3.6%
C2	*Seton et al.* [2012]	Moving hotspots 0–100 Ma [*O'Neill et al.*, 2005] TPW-corrected palaeomagnetic 100–200 Ma [*Steinberger and Torsvik*, 2008]	Not minimized in plate reconstruction. Minimized in the lower mantle by the low-viscosity asthenosphere in the dynamic model	1,0.1,1,100 1210 km 45° (<660 km) then 90° +3.6%

[a]Factor applied to reference viscosity (10^{21} Pa s) for mantle above 160 km (lithosphere), between 160 and 310 km (asthenosphere), between 310 and 410 km (upper mantle), and below 670 km (lower mantle).

[b]*Granot et al.* [2013] describes motion in the West Antarctic Rift System from Chron 18o (40.13 Ma) until around Chron 8o (26.5 Ma) [*Cande et al.*, 2000; *Granot et al.*, 2013]. A plate boundary likely existed between East and West Antarctic earlier in the Cenozoic, though the timing of extension is poorly constrained [*Cande et al.*, 2000; *Cande and Stock*, 2004]. For times earlier than Chron 18o we model extension within the West Antarctic Rift System using the C18o pole of rotation from *Granot et al.* [2013] but with a larger angle to minimize the amount of deformation implied in New Zealand, which is considered to be tectonically quiescent during this period [*Ballance*, 1993; *Sutherland*, 1995].

For comparison, a case was computed using the plate reconstruction of *Seton et al.* [2012] (case C2, Figures 3–5, S5, and S9 and Table 2) that is different for the Arctic and northern Panthalassa by way of a simpler regional tectonic history with fewer subduction zones, including the absence of intraoceanic subduction after 170 Ma (see panels at the top in Figures 3–5). Additional cases based on an alternative absolute reference frame, initial conditions, and mantle viscosity are discussed in the supporting information (Figures S3, S4, S6–S8, S10–S15 and Tables S2 and S3). These parameters do not significantly change the magnitude and trend of regional dynamic topography, which is the main focus of this paper (Figures 6–8, S11, S12, S14, and S15 and Tables S1 and S2).

In the initial condition (230 Ma, except for case C2 at 200 Ma), slabs associated with subduction zones that are thought to have already been in existence for more than ~50 Myr are included to a depth of 1210 km (or 1750 km for C3, see 230 Ma panels of Figure S10) to account for earlier subduction (Table 2). For subduction zones that are thought to have initiated less than ~50 Myr before 230 Ma, the initial slab depth is calculated from the estimated age of the subduction zone, assuming a sinking rate of 5 cm/yr in the upper mantle and 1.2 cm/yr in the lower mantle [*van der Meer et al*., 2010; *Butterworth et al*., 2014]. In the initial condition of case C1, the slab dip is 45° for depths $<$425 km and 90° for greater depths. Slabs are initially 3 times thicker in the more viscous lower mantle compared to the upper mantle. Time-dependent kinematic boundary conditions are exported from *GPlates* [*Boyden et al*., 2011] for our reconstructions, which include continuously closing plates in single million year increments [*Gurnis et al*., 2012]. Seafloor ages [*Seton et al*., 2012], tectonothermal ages [*Artemieva*, 2006], and the half-space cooling model [e.g., *Davis and Lister*, 1974] are used to generate the temperature structure of the lithosphere as in *Flament et al.* [2014]. The thermal structure of the subducting lithosphere, computed analytically assuming a slab dip of 45° for each million year increment, is assimilated with the mantle temperature field predicted by the geodynamic model within 350 km of subduction zones. This progressive assimilation aims to ensure that upper mantle slab buoyancy is consistent with the plate tectonic reconstruction and that subduction is asymmetric [*Bower et al*., 2013].

In our subduction-driven numerical mantle flow models, which include a dense basal layer, upwellings several thousands of kilometers across slowly rise in the lower mantle from the core-mantle boundary. Narrow plumes (conduits several hundreds of kilometers across) crossing the whole mantle do not occur. As a consequence, positive dynamic topography is due to passive return flow and positively buoyant deep upwellings along the CMB. For this reason the predicted dynamic topography highs are broader and of lower amplitude than predicted dynamic topography lows (Figures 6 and S11). Surface dynamic topography is obtained by restarting the model every 10 Myr with no-slip surface boundary conditions, which implies the mantle and plates to be strongly coupled, and only considering temperature and velocity variations below 350 km depth because data are progressively assimilated to this depth. Note that using free-slip boundary conditions, which implies little coupling between the mantle and plates, would significantly reduce the amplitude of the predicted dynamic topography [e.g., *Flament et al*., 2014] but have marginal effects on its long-wavelength pattern. We visually compare the predicted temperature fields, in which slabs are defined as 10% colder than background mantle temperature (0.45 contour of 0.5 ambient mantle, nondimensional), to three *S* wave seismic tomography models (*Grand* [2002], *Simmons et al*. [2010] GypsumS, *Ritsema et al.* [2010] S40RTS).

3. Predicted Mantle Structure

3.1. North America

An east-west profile through predicted mantle temperature at 30°N under North America (Figure 3, alternative cases Figure S7) shows a massive east-dipping slab (*e*) extending from ~600 to 2000 km depth under 90–60°W. This modeled slab corresponds to Farallon (and Cache Creek Ocean) lithosphere subducted along western North America. The match between predicted thermal structure and seismic tomography is good at 30°N, suggesting that anomaly (*e*) is mainly accounted for by east-dipping subduction along continental North America. The similarity of slab (*e*) between cases C1 and C2 (as well as C3–C5, Figure S7), despite differences in the plate reconstructions of *Seton et al.* [2012] and *Shephard et al.* [2013], reflects that subduction at 30°N was continental rather than intraoceanic. Based on maps of time-dependent model temperature at various depths (Figure S2), the smaller slabs (*a*) and (*c*) are related to slab migration from the north-northeast and are associated with subduction along the continental margin, largely before 150 Ma (see also Figures S3–S7).

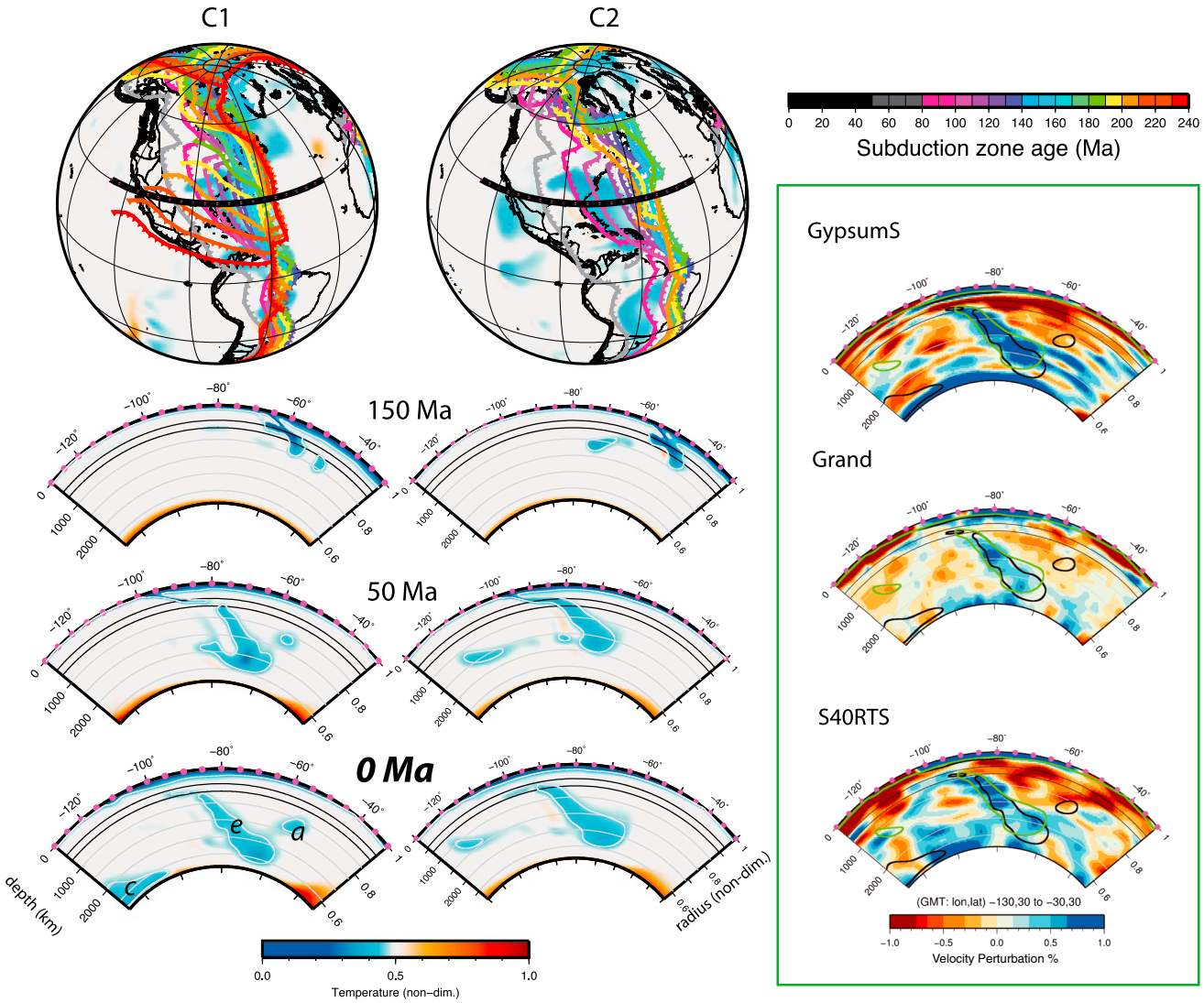

Figure 3. Predicted time-dependent mantle temperature for case C1, based on the plate reconstruction of *Shephard et al.* [2013], case C2, based on the reconstruction of *Seton et al.* [2012] (Table 2) and present-day comparison to seismic tomography. Panels at the top, orthographic projection of cross section at 30°N latitude across NAM (130–30°W) superimposed on location of subduction zones and predicted mantle temperature at ~1500 km depth. Dominant inferred slab from this vertical cross-section result from subduction along the northeastern margin of Panthalassa and continental North America (*e*). Slabs (*a*) and (*c*) are related to earlier subduction along continental margin, both of which have migrated within the mantle from the northeast. Panels on the right in green box, seismic velocity anomalies for three tomography models with 0.45 mantle temperature contours (10% colder than ambient mantle that has nondimensional temperature of 0.5) overlain for models C1 (black) and C2 (green).

A cross section of case C1 further north through 50°N (Figure S5) at present day shows Panthalassa slabs (Farallon, Izanagi, and Cache Creek plates) subducted along a continental margin and an intraoceanic convergent boundary (Figures 2 and S1). The present-day thermal structure for case C1 can be separated into four distinct slabs based on the time-dependent mantle evolution (labeled (*a*–*d*) in Figure S5, alternative cases Figures S6 and S14). The distinction of adjacent slabs of different age and subduction zones can be extrapolated to corresponding features within seismic tomography, which do not show linearly distinct velocity anomalies (cf. *Sigloch and Mihalynuk* [2013] discussion below).

The present-day slab (*a*) predicted by case C1 (Figure S5; ~1000–2200 km, 40–70°W, corresponds to slab (*g*) Figure 4) is related to subduction along the western North American margin since 230 Ma. The deep (>2000 km) thermal anomaly to the west ((*b*), 100–80°W, Figure 3) is associated with the subduction of oceanic lithosphere (Cache Creek and Farallon plates) along the intraoceanic Wrangellia Superterrane

until 140 Ma. The intraoceanic subduction of older lithosphere, compared to the contemporaneously subducting younger lithosphere farther east along North America (Figures 2, S1, and S5), might explain why this western slab (*b*) is overall deeper than slab (*a*). Slab (*c*) at the core-mantle boundary (CMB) (also in Figure 3) does not have any direct connection with the immediately overlying mantle or trench at this fixed latitude but migrated since at least 100 Ma through the lower mantle from the north-northeast toward its present location (Figures S2–S4). Overlying slab material in the upper mantle and uppermost lower mantle ((*d*), 80–90°W) is related to younger Farallon subduction (100–50 Ma).

Compared to seismic tomography, modeled slab (*a*) is offset (to the east) from the main "Farallon" slab seismic anomaly (70–90°W, ~1000 and 2000 km depth) by approximately 20° longitude. Furthermore, slab (*c*) lies at the CMB, deeper than the seismic tomography anomalies located at ~1500–2000 km depth (130–100°W), suggesting the lithosphere subducting along the Wrangellia Superterrane may be too old in these reconstructions. These offsets suggest that further refinement of the regional plate reconstruction around this latitude is required. Avenues to be tested (see also the apparent overprediction of slab (*g*) volume, Figure 4) include initiating subduction along North America later than 230 Ma, decreasing convergence rates and/or the age of subducting lithosphere, changing the timing and location of the intraoceanic subduction, and changing the absolute reference frame [see *Torsvik et al*., 2008; *Shephard et al*., 2012]. However, we note that the volume and depth of slab (*a*) are broadly consistent with tomography at this latitude, which is a marked improvement compared to C2 [*Seton et al*., 2012], and that the slab at 30°N matches seismic tomography well.

Our results suggest that slabs under North America at 50°N might be related to both Andean-style continental and intraoceanic subduction, despite the longitudinal offset to seismic tomography. Intraoceanic subduction along the Wrangellia arc was not included in the reference global reconstruction of *Seton et al.* [2012] despite geologic evidence for its activity prior to its accretion to North America (see *Shephard et al*. [2013] for a further discussion, *Nokleberg et al*. [2000], and *Trop et al*. [2002]). Therefore, case C2 (Figure 3) based on the *Seton et al.* [2012] reconstruction predicts fewer slabs under ~40–90°W than those cases based on *Shephard et al.* [2013] and is therefore even more difficult to reconcile with seismic tomography in this region.

The contrast in slab geometries between 50°N and 30°N as predicted by our numerical models can be attributed to latitudinal variations in subduction kinematics since 230 Ma; at ~30°N, the traditionally interpreted Farallon slab (slab (*e*)) [*Bunge and Grand*, 2000; *Grand et al*., 1997] represents lithosphere predominantly subducted along continental North America (Farallon and Cache Creek Ocean), whereas further north, the Farallon (slab (*a*)) represents two adjacent subduction zone settings including ocean-continent and intraoceanic subduction. Considering seismic tomography alone, the prominent east-dipping high-velocity seismic anomaly present at 30°N (Figure 3) is in contrast to the more longitudinally extensive seismic structure at 50°N (Figure S5), consistent with our interpretation of a latitudinal difference in subduction styles. However, our forward models suggest that there is scope for further refinement of the regional plate model, particularly in the northern regions (Figure S5). Future geodynamic models should test alternative subduction scenarios including variability in convergence rates and subduction polarities.

Our interpretation of a latitudinal variation in intraoceanic and Andean-style subduction to account for the present-day dominant lower mantle seismic structure under the U.S. East Coast is in contrast to a recent reconstruction of *Sigloch and Mihalynuk* [2013]. They suggested that this seismic anomaly is one massive structure formed by a long-lived, stable intraoceanic subduction system that dipped to the west until it collided with the westward moving North America. In their reconstruction, the "Cascadia" slab under ~100–120°W is connected to the present-day trench and represents east-dipping Farallon lithosphere. Our study suggests that a long-lived, stable intraoceanic trench is not necessary to account for the Farallon slab (slab (*e*), Figures 3 and S7) and is rather explained by variation in intraoceanic and continent-ocean subduction (slabs (*a* and *e*), Figures S5–S7). Significantly, the reconstruction of *Sigloch and Mihalynuk* [2013] is largely based on a high-resolution *P* wave tomography model that shows the Farallon slab to be a massive wall-like slab down to ~1800 km depth under the continental part of North America. However, the resolution of this tomography model is poor under the oceanic part of North America [*Sigloch*, 2011] and is also poor within the lowermost mantle and the deeper part of the Farallon slab. Their interpretation of a long-lived west-dipping intraoceanic subduction zone, rather than successive or migrating subduction

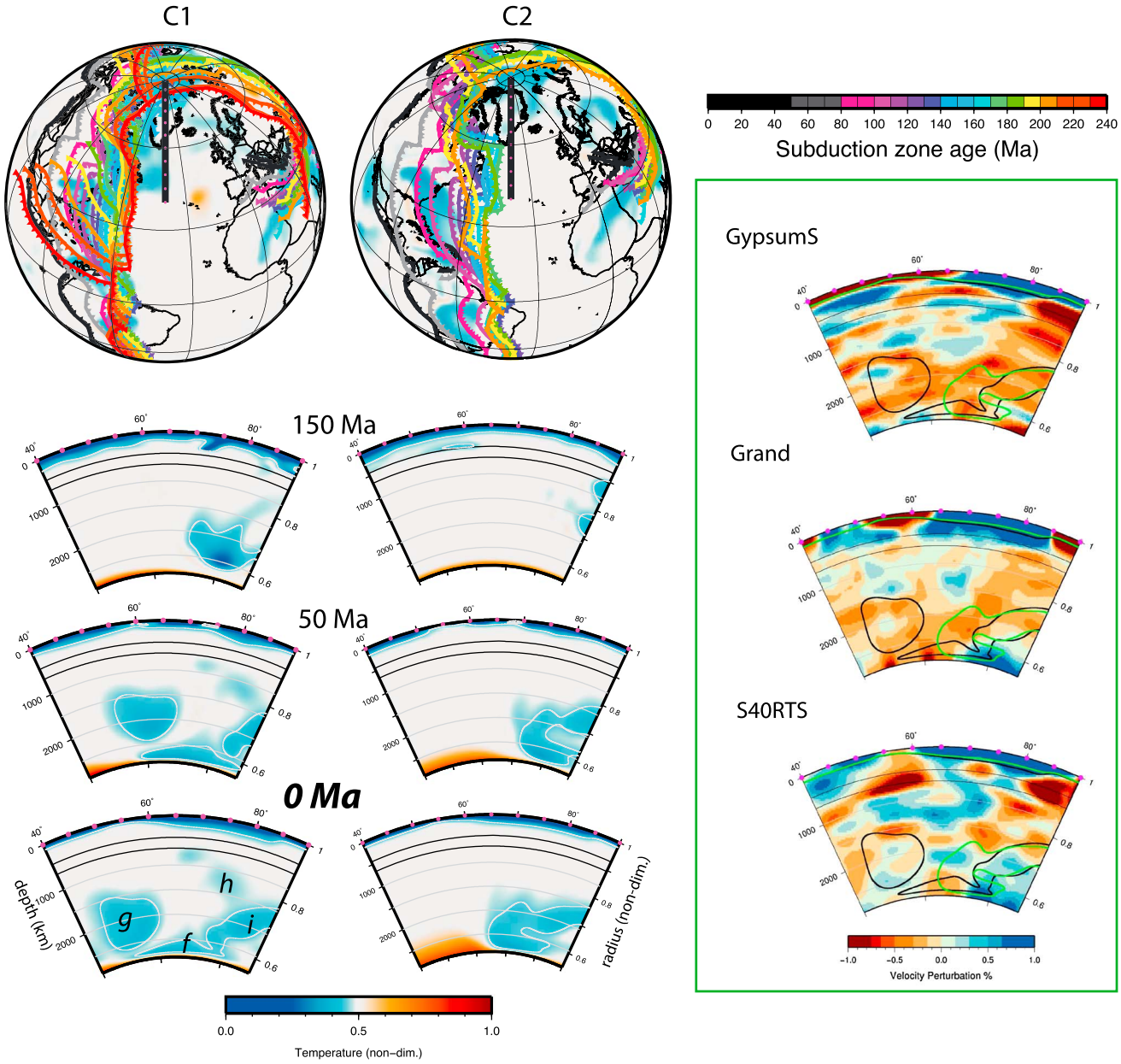

Figure 4. As for Figure 3 but for a cross section at 40°W longitude through Greenland and the North Atlantic (40–90°N). Inferred slabs within this cross section largely result from subduction along the northeastern margins of Panthalassa ((*g*), corresponding to slab (*a*) in Figure S5), Mongol-Okhotsk (*f*), South Anuyi Ocean (*h*), and northwestern Panthalassa (*i*).

zones, would likely not facilitate a break in the slab, in contrast to our reconstruction. Testing the subduction history of *Sigloch and Mihalynuk* [2013] in a geodynamic model will be of interest to future work, particularly to robustly explain the complex mantle structure north of ~50°N.

3.2. Greenland

A latitudinal vertical cross section under present-day Greenland at 40°W (Figures 4 and S8) for case C1 captures four slabs from Panthalassa, the Mongol-Okhotsk, and South Anuyi oceans (*f*–*i*). In our plate reconstruction, the Mongol-Okhotsk slab initiated prior to 230 Ma (230 Ma panel, Figure S10) and constitutes part of the present-day material on the CMB (*f*). Slab (*g*) at 40–60°N entered this profile from the west-northwest (Figure S2) and is related to subduction along north-northeastern Panthalassa

(corresponds to slab (*a*), Figure S5). The shallower part of the cold material (*i*) is related to migrating slabs from subduction along northwestern Panthalassa and the easternmost junction with the Mongol-Okhotsk subduction zone.

The present-day cold feature (*h*) at ~70–75°N, 1000–1500 km, can be attributed to South Anuyi Ocean subduction since the Late Jurassic based on the analysis of time-dependent vertical and horizontal profiles (Figures 4 and S2). This mantle region is complex due to subduction along the long-lived Panthalassa and Mongol-Okhotsk subduction zones as well as shorter-lived high Arctic subduction zones (slab (*h*)). This makes the history of the subducted Oimyakon Ocean difficult to decipher in the models, as it is reconstructed to have been subducted within ~1000 km of the northern Panthalassa margin (Figures 2 and S1).

Comparing predicted temperature to seismic tomography (Figure 4), the shallow (<1000–1500 km) slab, interpreted as the South Anuyi Ocean (*h*), is close to the relatively shallow (440–1500 km depending on tomography model), high-velocity anomalies at ~50-70°N. This was first suggested in *Shephard et al.* [2013] based on the absolute positioning of subduction zones through time. Similarly, while greater in depth and latitudinal extent in the model, Panthalassa slabs might explain the seismic anomaly in the deepest lower mantle between 80°N and 90°N. This is particularly evident in *Ritsema et al.* [2010] and to a lesser extent in *Grand* [2002].

While case C2 also predicts a deep slab associated with long-lived Panthalassa subduction, it does not predict the shallower midmantle slab, due to the lack of a South Anuyi Ocean subduction zone, and therefore arguably does not match seismic tomography as well. This suggests that the addition of circum-Arctic subduction in *Shephard et al.* [2013] constitutes an improvement of the reference global reconstruction and supports the hypothesis that the opening of the Amerasia Basin is linked to the subduction of a South Anuyi Ocean around the Late Jurassic to Early Cretaceous (~160–120 Ma).

This section also illustrates the aggregation and rise of compositionally denser, hot material in our model (e.g., Figure 4, C2 at 40–60°N, Figure 5 at 40–70°E). While plumes are not explicitly modeled to erupt at specific locations (e.g., from reconstructed LIP eruption sites), these upwellings are related to flow induced by slabs as they approach the CMB. This is an important observation in the context of Large Low Shear wave Velocity Provinces (LLSVP) formation and stability and suggests a possible interaction of long-lived slab graveyards migrating and perturbing "plume generation zones" [e.g., *Burke et al*., 2008; *McNamara and Zhong*, 2005; *Bower et al*., 2013]. These zones of accumulating deep hot material correspond to dynamic topography highs under Africa and the Pacific (2823 km depth, Figures S2 and S3).

3.3. Northern Eurasia

The evolution of the Mongol-Okhotsk (MOK) slab (*m*) produced by case C1 can be seen through 60°N latitude and 0–100°E longitude (Figure 5). This profile, unlike those in Figures 3 and 4, captures a single, relatively isolated subduction zone such that adjacent slabs do not complicate the present-day mantle structure. From 230 Ma, the modeled MOK slab sinks and thickens by advection and by present-day it is largely located west of 30°E. The slab feature that appears from the east of the profile (*p*) and that by 0 Ma is located east of 85°E longitude is here related to subduction along northwestern Panthalassa (predominantly Izanagi slab, Figure S9). Case C2 also predicts two distinct slabs, with the MOK slab, (*m*), located slightly shallower (<2500 km depth) and to the east (up to 45°E longitude) compared to case C1.

Seismic tomography at 60°N (0–100°E) reveals two deep, seismically fast anomalies (Figure 5): a dominant seismically fast anomaly at 60–100°E, largely corresponding to model slab (*p*), and a second less pervasive slab, corresponding to model slab (*m*), between 0 and 35°E longitude. Previous interpretations of seismic tomography by *van der Voo et al.* [1999] and *van der Meer et al.* [2010] attributed the MOK slab to a large seismic anomaly located no further west than 100°E and 60°E longitude, respectively (corresponding to model slab (*p*)). This is in stark contrast to our results that predict the slab associated with MOK subduction (from the Late Permian until 150 Ma [*Seton et al*., 2012]) to be located no farther east than 35°E (slab (*m*), Figure 5) and that subducted Panthalassa lithosphere (*p*) accounts for the previously interpreted MOK slab from seismic tomography. Our reinterpretation of the MOK slab location holds implications for absolute reference frames that apply a longitudinal correction based on such "anchor" slabs [e.g., *van der Meer et al*., 2010].

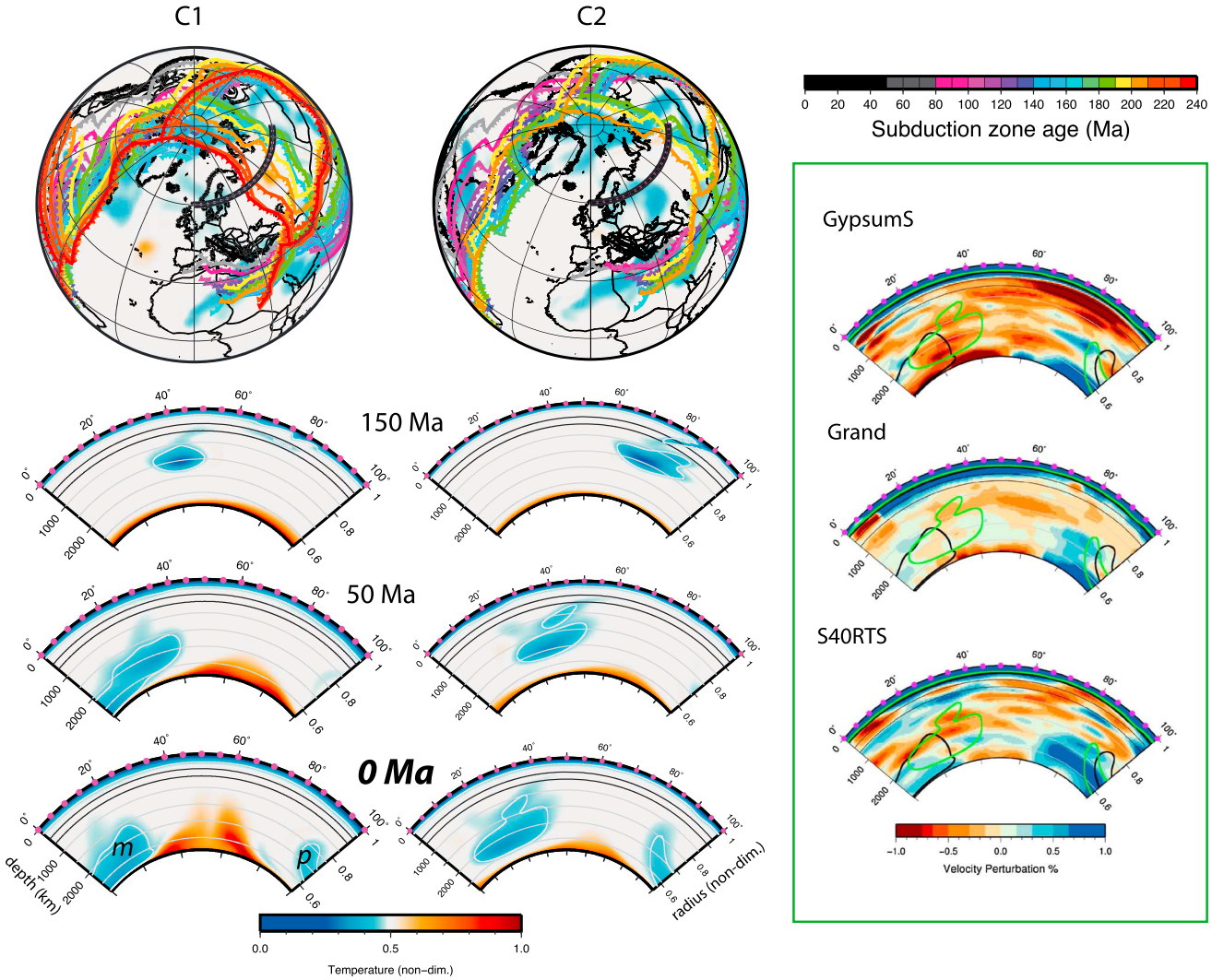

Figure 5. As for Figure 3 but for a cross section at 60°N longitude through northern Eurasia (0–100°E). Note that 1° of longitude corresponds to 0.5 arc degrees. Inferred slabs within this cross section largely result from subduction along the northern margin of the Mongol-Okhotsk Ocean (*m*) and along the northwestern margin of Panthalassa (*p*).

There are several assumptions in our coupled plate-mantle model that could account for this offset. (1) Despite being minimized, NLR (Figure S13) may still lead to excess lateral mantle flow that may be exacerbated for long-lived, north-south trending subduction zones such as the MOK. While NLR is large (>0.44°/Myr at times, Figure S13) in the reconstruction used for case C2, this case includes an asthenosphere which decouples the lithosphere from the deeper mantle, and predicts the MOK slab to be no farther east than 45°E. Case C1, in which NLR is minimized in the plate reconstruction, predicts the MOK slab west of 35°E. Hence, minimizing NLR does not reconcile the MOK slab to that previously inferred from seismic tomography, suggesting that this is a robust feature, independent of the differences in subduction zone location introduced by alternative absolute reference frames. (2) The absolute reference frame is at least ~20° off in longitude before 150 Ma so that the MOK subduction zone should be shifted to the east; however, this may exacerbate NLR and lead to mismatches along the North American margin and elsewhere. (3) The relative plate reconstructions of MOK subduction are inaccurate in time (initiation and/or duration of subduction) and/or location. Further modeling is required to investigate these points and to improve the match between the predicted thermal anomaly and seismic anomaly. Nevertheless, our results suggest that the MOK slab may currently be located farther west than previously thought and that the previously interpreted MOK slab is instead related to long-lived subduction along northwestern Panthalassa.

4. Dynamic Topography

4.1. Predicted Dynamic Topography

Time-dependent maps of circum-Arctic dynamic topography (Figures 6 and S11) reflect its global degree 2 pattern; two dynamic topography highs (related in our model to both passive return flow and positively buoyant deep upwellings along the CMB) corresponding to the northern part of the African and Pacific Large Low Shear wave Velocity Provinces (LLSVPs), which are separated by an evolving but long-lived circum-Pacific dynamic topography low (related to sinking slabs). Lows predicted elsewhere [see *Flament et al*., 2013] match spatially to those previously discussed under the Americas [e.g., *Spasojevic et al*., 2008] and Southeast Asia [e.g., *Wheeler and White*, 2000]. We restrict the analysis for dynamic topography case C1 that better predicts circum-Arctic lower mantle structure than case C2.

At 170 Ma there is a broad dynamic topography low of up to −1500 m adjacent to the Mongol-Okhotsk, western Panthalassa, and Tethyan subduction zones (Figure 6). At these times, much of the circum-Arctic is located within neutral to slightly positive (0–200 m) dynamic topography, with the exception of distal Siberian regions, which are separated from North America by the South Anuyi Ocean (Figures 2 and S1) and are located above a dynamic topography low. By 150 Ma, a dynamic topography low is caused by the active consumption of the Oimyakon and South Anuyi oceans and continued subduction along northern Mongol-Okhotsk and Panthalassa (Figures 2, 6, S1, and S11). At this time, the Siberian terranes still overlie this dynamic topography low, whereas much of the present-day Arctic (including Greenland) is located farther away to the south and east where dynamic topography is positive. By 120 Ma, the Amerasia Basin had largely opened and subduction in the circum-Arctic became largely restricted to northern Panthalassa [*Shephard et al*., 2013].

Later in time, the magnitude of negative dynamic topography generally decreases from < -1200 m to -1000 m, and the dynamic topography lows broaden to form at present-day a band ~4500 km wide, running from North America, through the North Pole toward East Asia. As a result, an increasing proportion of the circum-Arctic is subjected to negative dynamic topography through time as previously noted in the context of supercontinent formation and dispersal cycles [*Gurnis and Zhong*, 1991]. With the opening of the Atlantic Ocean and Amerasia Basin, various circum-Arctic terranes are dispersed and generally move west, toward mantle downwellings. The majority of Eurasia (including present-day Russia) remains located over a broad dynamic topography low.

The time-dependent change in dynamic topography at a particular location enables an investigation of vertical motions in the plate frame of reference. The evolution of dynamic topography sampled at selected circum-Arctic locations (Figures 1 and 7; Tables S1 and S2 and Figure S12 for alternative cases) reveals two major trends across the region: broad subsidence from at least 170 Ma to ~70–50 Ma, followed by either slowed subsidence or uplift until the present. We limit this analysis to times after 170 Ma because it takes ~50 Myr for dynamic topography to reach a dynamic equilibrium from the synthetic initial condition [*Flament et al*., 2014].

4.2. Dynamic Topography Changes—Comparison to Observables

4.2.1. Svalbard and Barents Sea Region

Subsidence since the Devonian has been noted in several Arctic regions, including Svalbard [*Dörr et al*., 2013] (Figure 1) where a pseudo-backstripped well-revealed rapid basement subsidence from the Late Devonian to the earliest Triassic (~360–250 Ma, ~700 m, ~7.8 m/Myr) that slowed in the Early Triassic to Late Jurassic (~250–157 Ma, ~200 m, ~2.2 m/Myr), accelerated in Late Jurassic to mid-Cretaceous (~157–100 Ma, ~400 m, ~7.0 m/Myr) and was followed by a hiatus until the Palaeogene and subsequent uplift (Figure 7e and below). Case C1 (Table S1) predicts an average subsidence rate of ~7.4 m/Myr of Svalbard (orange curve and stars, Figures 1 and 7a) from 170 to 100 Ma. This is consistent with the ~7.0 m/Myr derived from *Dörr et al.* [2013] and is illustrated by the reasonable match in the trend of our modeled dynamic topography and a hypothetical section (backstripped "pseudo-well") from *Dörr et al.* [2013] from ~170 to 100 Ma (Figures 1 and 7e). The mismatch for younger times suggests that uplift is not driven by long-wavelength slab-driven dynamic topography (see below). Similarly, from our model results, Fennoscandia (yellow, Figures 1 and 7a) and Franz Josef Land (green, Figures 1 and 7a) show consistent subsidence from 170 to 50 Ma of up to 4.7 m/Myr and 5.9 m/Myr, respectively, for C1.

For the adjacent East Barents Sea sedimentary basin, *Gac et al.* [2012] summarized the water-loaded subsidence history as follows: subsidence from the early Palaeozoic (2–3 km of Carboniferous sediments), acceleration during the Late Permian and Early Triassic (>12 km sedimentary succession), "very low

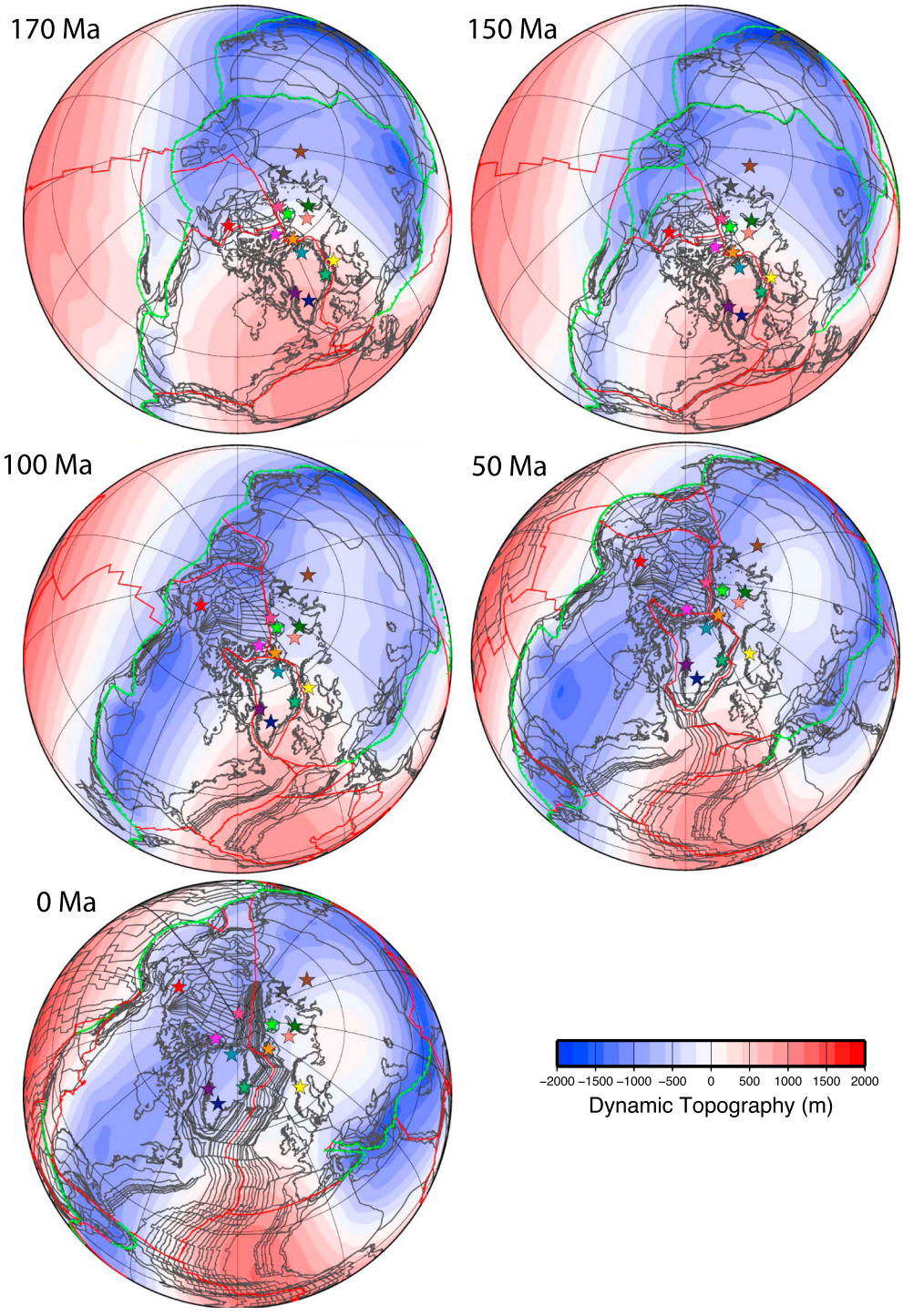

Figure 6. Air-loaded surface dynamic topography predicted by case C1 between 170 and 0 Ma. Results for cases C3–C5 are shown in the supporting information Figure S11. Reconstructed coastlines in grey, ridge and transform plate boundaries in red, and subduction zones in green. Stars indicate location of selected reconstructed Arctic points as in Figure 1. Orthographic projection centered on 30°W.

subsidence rates" until the Cenozoic (4–5 km Jurassic and Cretaceous sediments) which was followed by uplift. Total subsidence of more than 16 km is inferred to have occurred since the base of the Carboniferous in the deepest parts of the basin, and up to ~3 km on the basin flanks. Based on the inference that the gravity signal indicates that the lithosphere is in isostatic balance at present day, *Gac et al.* [2012] suggested

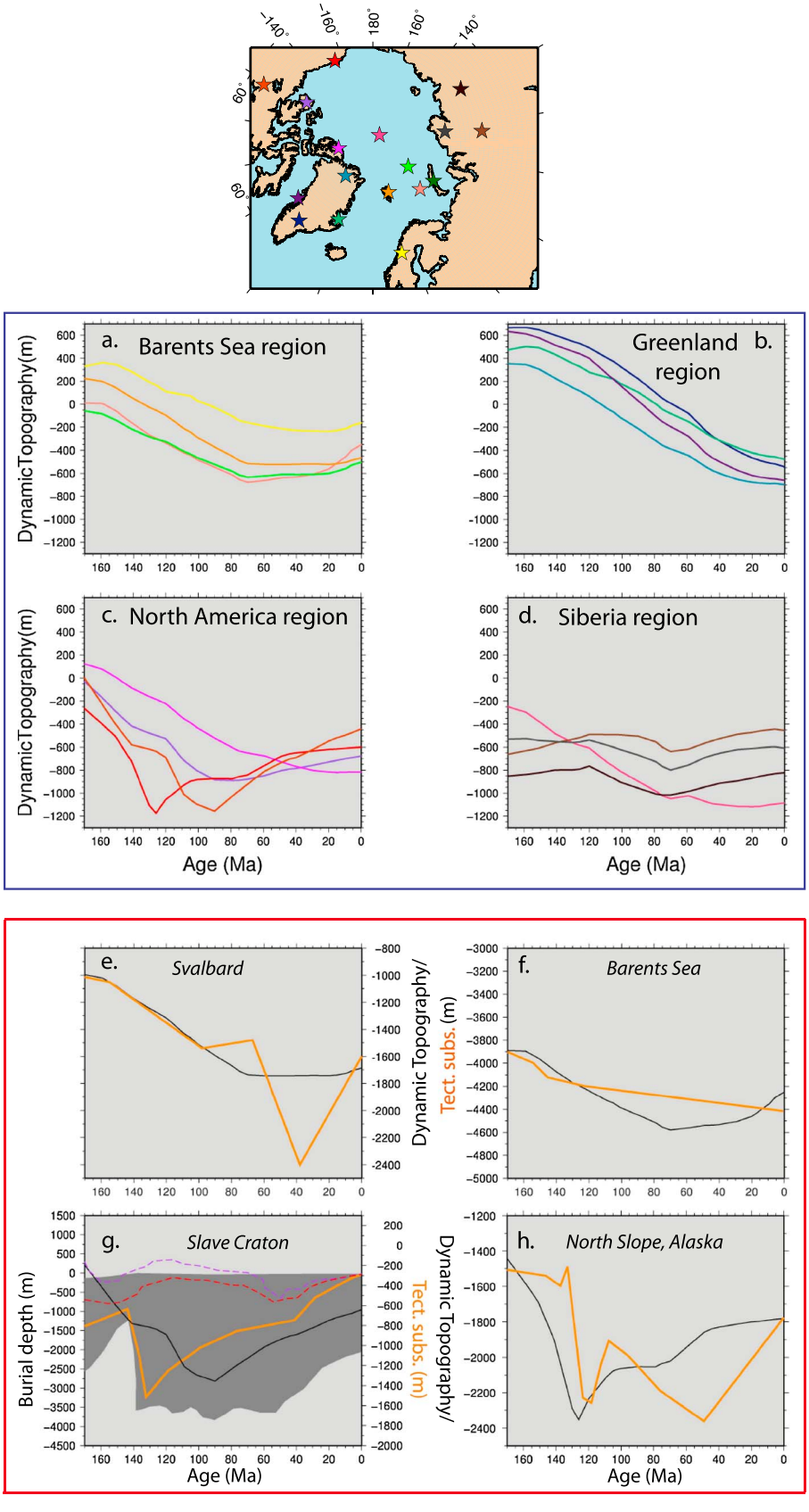

Figure 7

that continued and significant subsidence could be attributed to mass excess from magmatic underplating, which increased in density through the Permian to Triassic. *Gac et al.* [2013] further suggested that lithospheric shortening from the closure of the Uralian Ocean, east of Novaya Zemlya, during the Late Permian to Triassic is the trigger for the continued "densification" of this mafic body.

While our model starts later than the Devonian to Triassic phase of subsidence described for the Barents region, we suggest that mantle-driven dynamic topography might have contributed to the continuation of Late Jurassic to mid-Cretaceous subsidence. Indeed, case C1 (peach, Figures 1 and 7a) might account for part of the Late Mesozoic to Cenozoic phase of subsidence with 7.1 and 3.1 m/Myr of water-loaded subsidence predicted between 170–100 and 100–50 Ma, respectively (Table S1). Figure 7f shows a good match between independently derived tectonic subsidence [*Gac et al*., 2013] and predicted dynamic subsidence from our models between ~170 and 100 Ma. We suggest that for that period, dynamic subsidence is an alternative or complementary mechanism to the densification of an underplating magmatic body by phase change [*Gac et al*., 2012, 2013] and can adequately explain the continued subsidence of the basin until ~100 Ma.

The long-lived subsidence, as predicted by our models for the Barents Sea and adjacent regions (Table S1 and Figures 1 and 7a), either slows down or reverses to uplift around the Early Cenozoic. Since 50 Ma, an uplift rate of 1.2 m/Myr is predicted for Svalbard and Fennoscandia and 2.2 m/Myr for Franz Josef Land. Similarly, the Barents Sea reverses to uplift of 5.9 m/Myr from ~50 Ma. This reversal in predicted dynamic topography is interesting as Cenozoic uplift of $<$1 km to $>$3 km, erosion and exhumation around much of the North Atlantic and Arctic have gained much recent attention in independent literature [e.g., *Vågnes et al*., 1992; *Skogseid et al*., 1992; *Japsen and Chalmers*, 2000; *Crosby et al*., 2008; *Anell et al*., 2009]. Apparent northward propagation of North Atlantic uplift has been linked to north to northwestward Atlantic rift axis propagation [*Lundin and Doré*, 1997; *Doré et al*., 1999]. North Atlantic opening including rift-flank uplift and magmatic underplating, North Atlantic Igneous Province (NAIP, Figure 1) related activity and possible plume ascent are favored by many authors to explain the late Paleocene to early Eocene uplift [e.g., *Stuevold et al*., 1992; *Clift and Turner*, 1998; *Anell et al*., 2009]. The most recent phase of uplift, 5–0 Ma, is largely attributed to glacioisostatic rebound [e.g., *Fjeldskaar et al*., 2000; *Anell et al*., 2009]. However, many aspects of this uplift history remain to be resolved, including constraining the timing and magnitude of uplift, accounting for the apparent multistage uplift histories, and reconciling contemporaneous observations of subsidence, especially in offshore areas [*Poag and Sevon*, 1989; *Japsen and Chalmers*, 2000; *Doré et al*., 2002; *Scheck-Wenderoth et al*., 2007]. *Green and Duddy* [2010] reiterated that contemporaneous Cenozoic exhumation could be correlated from North Slope of Alaska, Canadian Arctic Islands, and North Atlantic. They stress that the synchronicity and vast spatial scales requires "plate-scale" mechanism(s), which to date had not been adequately explored. It is apparent that no single mechanism or observation can explain the vertical motions, and it is likely a combination of plate- and mantle-scale dynamics. Additionally, a stratigraphic hiatus from ~44 to 18 Ma from a core of the Lomonosov Ridge has been attributed to postrift uplift and erosion due to opening of the Eurasia Basin and associated lithospheric thinning and mineral composition changes [*Moran et al*., 2006; *Backman et al*., 2008; *Minakov and Podladchikov*, 2012]. For the Lomonosov Ridge, case C1 (pink, Figures 1 and 7d) predicts (water-loaded) subsidence from 170 to

Figure 7. (a–d) Evolution of modeled dynamic topography since 170 Ma at selected circum-Arctic locations (based on the plate reconstruction) grouped into four geographic regions. The colors of the plotted lines match the colors of the stars in the top map inset (also Figure 1). Note the broad subsidence predicted for most locations from 170 Ma to between ~70 and 50 Ma followed by slowed subsidence or uplift to present day. Values are given in Table S1. Air-loaded results shown for all locations except for Lomonosov Ridge (in "Siberia region") and Barents Sea which are water loaded. Results for cases C3–C5 are shown in the supporting information Figure S12 and Table S2. (e–g) Comparison between predicted dynamic topography from case C1 (black) and independent constraints (thick orange) at selected circum-Arctic locations (see Figure 1). (Figure 7e) Svalbard, comparison to backstripped pseudoborehole analysis from *Dörr et al.* [2013] (predicted depths to basement, corrected for sediment loading, water depth, and sea level changes). (Figure 7f) East Barents Sea, tectonic subsidence curve as presented in *Gac et al.* [2012, 2013] (water-loaded subsidence). (Figure 7g) Slave Craton, two independent models of dynamic topography pink (TG1) and red (TG3) from *Zhang et al.* [2012] and "best fit" burial-unroofing history from thermochronology in orange from *Flowers et al.* [2012] (their range of inverse modeling simulation results in shaded grey). (h) North Slope of Alaska, tectonic subsidence curve from the Colville Basin, *Cole et al.* [1997]. For comparison, we have shifted the predicted dynamic topography at Svalbard −1220 m, Barents Sea −3900 m, Slave Craton −200 m, and North Slope −1180 m, respectively.

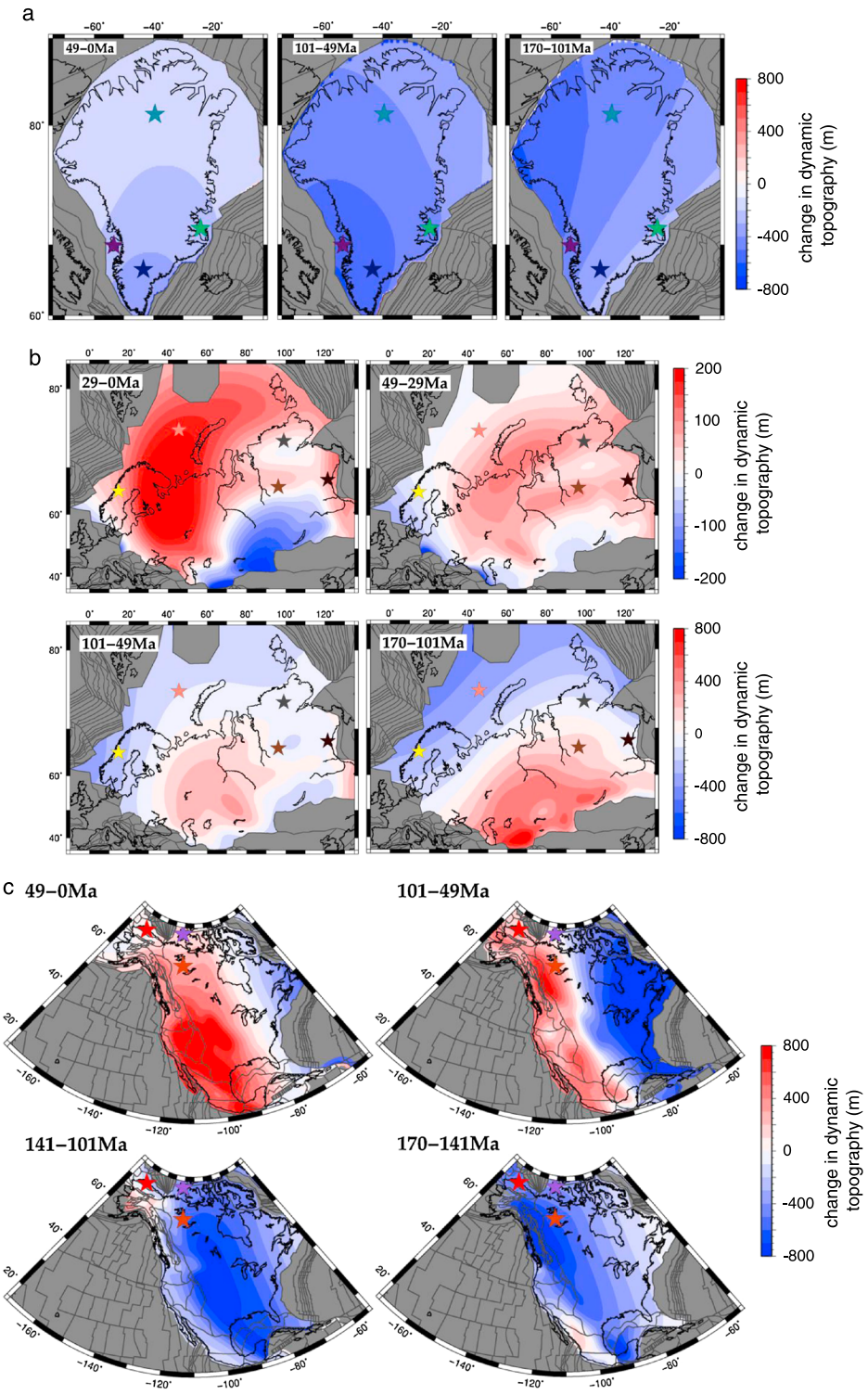

Figure 8. (a) Change in air-loaded dynamic topography predicted by case C1 across Greenland (fixed reference frame). Differential dynamic topography for three time intervals 170–101, 101–49, and 49–0 Ma reveals an evolving changing tilt of the continent from toward the west, to southwest, and south, respectively. Note that our models do not include active plumes in the upper mantle, which likely contribute to the observed Cretaceous uplift of Greenland not predicted here, see in text. Colored stars identify selected locations, also shown in Figures 1, 6 and 7. (b) Change in air-loaded dynamic topography predicted by case C1 across Siberia and Eurasia (fixed reference frame) for four time intervals 170–101, 101–49, 49–29, and 29–0 Ma. (c) Change in air-loaded dynamic topography predicted by case C1 across North America for four time intervals 170–141, 141–101, 101–49, and 49–0 Ma.

50 Ma at an average rate of 6.8 m/Myr, which slows to an average subsidence rate of 1.4 m/Myr for the period 50–20 Ma, the uplift of 1.6 m/Myr since 20 Ma.

While coincident in Cenozoic timing, the predicted dynamic uplift from our models (typically <4 m/Myr in the Barents region) is not of the same magnitude as constrained by independent data (e.g., Figure 7f), pointing to other processes to explain the most recent uplift history the area. Our focus on subducted slabs as opposed to active mantle plumes may also explain our predictions for Greenland. Based on our results, Greenland is modeled to be a region of long-lived subsidence throughout the time span of case C1, with rates of ~3.3–11.2 m/Myr (Table S1 and Figures 1, 7b, and 8) and the fastest period between 100 and 50 Ma (8.1–11.2 m/Myr). An investigation of differential dynamic topography across Greenland (Figure 8) points to overall tilting due to subduction from ~170 to 100 Ma toward the west, from ~100 to 50 Ma to the southwest and ~50 Ma to present day to the south. Case C1 (pink, Figures 1 and 7c and Table S1) predicts subsidence of up to 10.7 m/Myr from 170 to 50 Ma for Ellesmere Island, adjacent to Greenland. Moving farther west, Banks Island (purple, Figures 1 and 7c) illustrates a reversal from subsidence (of <11 m/Myr) to uplift of 2.6 m/Myr around 50 Ma.

4.2.2. Slave Craton

Flowers et al. [2012] discussed vertical motions of the western Canadian Shield based on thermochronology and concluded that subsidence before 350 Ma and uplift from 350 and 250 Ma could be attributed to dynamic topography imparted by deep mantle flow. For more recent times, their inverse thermal models show a period of rapid temperature increase (burial) around 150 Ma followed by protracted unroofing to present day (also presented in *Zhang et al.* [2012]; Figure 7g). Case C1 predicts relatively rapid subsidence around the Slave Craton (dark orange, Figures 1 and 7g; Table S1) of ~14.5 m/Myr until ~90 Ma, followed by uplift of up to 8 m/Myr until present day. While still in the range (grey polygon) of the thermochronology data, the predicted shift from rapid subsidence to uplift (at ~90 Ma) is delayed by ~50 Myr compared to the best fit to thermochronology (~140 Ma) [*Zhang et al*., 2012; *Flowers et al*., 2012]. This temporal offset might indicate discrepancies between the location of the overriding plate and the position of the underlying subducted slabs. Our choice of absolute reference frame may result in the Slave Craton (North America) being too far east relative to the underlying mantle around 140 Ma. Alternatively, subduction prior to 140 Ma may occur too far west in the reconstruction. Further uncertainty may be associated with relative plate motions, since the 130–90 Ma period coincides with a main phase of opening within the Mid- and North Atlantic. Despite these limitations, the dynamic topography predicted by our model for ages <150 Ma is closer to the thermochronology constraint than that predicted by the model of *Zhang et al.* [2012]. If the vertical motions of the Slave Craton are indeed due to mantle flow, they could be used as a robust constraint to refine future regional tectonic reconstructions.

4.2.3. West Siberian Basin

The tectonic subsidence of the West Siberian Basin (Figure 1) is characterized by a period of rapid subsidence (~50 m/Myr) between ~210 and 200 Ma followed by 1 km of protracted subsidence until the Late Cretaceous [*Galushkin et al*., 1999]. Six backstripped wells within the West Siberian Basin [*Saunders et al*., 2005], revealed less subsidence than predicted by a steady state cooling model between 240 and 190 Ma (for a stretching factor of 1.62), followed by greater subsidence than predicted after 190 Ma. Building on this, *Holt et al.* [2012] suggested that such delayed early Mesozoic subsidence observed in the West Siberian Basin [*Saunders et al*., 2005] could be robustly explained by the waning of a plume head. Furthermore, an apparent northward tilt of the West Siberian Basin basement surface matches the greatest subsidence and is correlated with the most extension [*Saunders et al*., 2005]. However, the increased subsidence after 250 Ma within the West Siberian Basin may be restricted to the north-northeastern region of the basin [*Vyssotski et al*., 2006]. The apparent lack of subsidence in the East Siberian Platform has been attributed to buoyancy of the Archean and early Proterozoic lithospheric mantle [*Artemieva and Mooney*, 2001; *Vyssotski et al*., 2006].

Unlike the aforementioned regions of the circum-Arctic, Siberia does not show a consistent trend of anomalous subsidence or uplift within our model. An evolving low-magnitude signal (<300 m; ±2.5 m/Myr) of uplift-subsidence-uplift separated at approximately 120 and 70 Ma, respectively, is predicted by C1 for the Siberian Traps (light brown, Figures 1 and 7d) and farther east in Siberia (dark brown, Figures 1 and 7d). This relatively weak signal reflects the absence of significant motion of Siberia that consequentially remains located broadly within a dynamic topography low throughout the evolution of the model. Comparing change in dynamic topography (Figure 8), a dominant regional tilt change toward the north can be inferred

until ~100 Ma whereby a subrounded pattern of uplift is modeled in the central onshore region. This uplifting region corresponds to a hot thermal feature predicted in our models around 2000 km depth (Figures S2 and S3). The uplift might also be related to a slower than average seismic velocity "Perm" anomaly inferred from seismic tomography, which is thought to extend ~500 km upward (~2400 km depth) from the CMB [*Lekic et al*., 2012]. Between 49–29 Ma and 29–0 Ma, uplift dominates northern Eurasia and Siberia, and the overall tilt shifts toward the west and south, respectively. These modeled changes in tilts are in contrast to the Cenozoic easterly tilt of Siberia modeled by geomorphic studies [*Allen and Davies*, 2007] and a plate-mantle model study, which included upper mantle upwellings [*Spasojevic and Gurnis*, 2012] and should be considered in future studies. From our models, the nearby Taimyr Peninsula (grey, Figures 1 and 7d) does show a reversal from subsidence of 1.3 m/Myr from ~170 to 60 Ma to uplift until present day of ~1.7 m/Myr, although of similarly low amplitudes.

4.2.4. North Slope

The evolution of the North Slope of Alaska from case C1 (red, Figures 1, 7c, and 8c) is characterized by one phase of relatively rapid subsidence from 170 to 130 Ma (~21 m/Myr) that reverses to ~4 m/Myr of uplift from ~130 Ma. The early subsidence is driven by the opening of the southern part of the Amerasia Basin (142.5–126 Ma) [*Alvey et al*., 2008; *Shephard et al*., 2013] and the motion of the North Slope over underlying Jurassic slabs (Figures 2 and S1). This evolution might explain why Alaska is topographically lower than the rest of the continental subduction front along North America [*Liu et al*., 2009]. Indeed, the amplitude of the early rapid subsidence is greater than that of the subsequent uplift. A tectonic subsidence curve from the Colville Basin from *Cole et al.* [1997] demonstrates rapid subsidence around 130 Ma (Figure 7h) but attribute this to flexure from the emplacement and imbrication of an allochthonous terrane. However, the good agreement in magnitude and timing between tectonic subsidence and predicted dynamic subsidence (Figures 7h and 8c) suggests a link to the opening of the Amerasia Basin and motion of the North Slope over sinking slabs may explain much of the topographic evolution of this region. Other features, including subsidence between ~100 and 60 Ma, and the uplift at ~130 Ma (Figure 7h), are possibly due to other tectonic processes or upper mantle flow.

Rapid uplift (exhumation of 6 km over 40 Myr) is recorded from 135 to 95 Ma along the Brooks Range (within geographical domain of the North Slope), which *Blythe et al.* [2010] correlate to opening of the Amerasia Basin opening and subduction along southern Alaska. Alternatively, *Cole et al.* [1997] propose isostatic rebound and unroofing from earlier allochthon emplacement (or alternatively thermal re-equilibration and expansion of earlier subducted lithosphere) to have caused the uplift during the Albian time. Our dynamic topography also predicts this timing of uplift and instead suggests the rebound of the North Slope to be at least partly due to its motion over and past sinking Jurassic slabs and/or the formation of a slab window from ridge subduction (Figure S1). Analogous slab-driven rebound of northwestern South America was proposed by *Shephard et al.* [2010]. While *Cole et al.* [1997] propose a second phase of subsidence from ~110 to 60 Ma due to "minor" thrusting and flexural loading from the south, inconsistent with our model (Figure 7h), other stratigraphic observations [*Wilson et al*., 1999] suggest rapid regional uplift of the Alaskan Peninsula during the mid-Cretaceous (Aptian to Santonian, ~125–84 Ma). Nonetheless, our prediction of uplift within the North Slope by 50 Ma, supported by geological observations [*Cole et al*., 1997; *Green and Duddy,* 2010] coincides with a period of uplift at 60 Ma throughout the Brooks Range and northern Alaska, which has previously been attributed to shallow subduction of the Kula Plate [*Blythe et al*., 2010]. Our findings are the first to explicitly link dynamic topography to Cretaceous vertical motion of the North Slope of Alaska.

5. Conclusion

We presented a global mantle flow model assimilating data from a recent plate tectonic reconstruction for the circum-Arctic since 230 Ma. At present day, the majority of inferred slabs under the circum-Arctic are relicts of Panthalassa and the Mongol-Okhotsk Ocean, subducted since the start of the Jurassic, with a smaller contribution of the South Anuyi and possibly Oimyakon Ocean basins. A comparison to seismic tomography yields variable fits between predicted cold slabs and fast seismic anomalies, which we attribute to a combination of the poor resolution of seismic tomography under the Arctic and uncertainties of the coupled plate-mantle model. In our forward model the massive Farallon slab under eastern North America [*Bunge and Grand*, 2000; *Grand et al*., 1997] represents several phases of subduction since 230 Ma. The model

predicts latitudinal variation in slab structure, with both intraoceanic subduction and ocean-continental subduction around 50°N and predominantly Andean-style ocean-continent subduction farther south around 30°N. We also suggest here for the first time that the Mongol-Okhotsk slab could lie at longitudes closer to 30°E rather than 60–100°E as previously proposed [e.g., *Van der Voo et al*., 1999; *Van der Meer et al*., 2010] and that the high-velocity material imaged by seismic tomography under 100°E is instead related to long-lived subduction along northwestern Panthalassa.

Comparing two cases based on different plate reconstructions [*Seton et al*., 2012; *Shephard et al*., 2013] to seismic tomography illustrates the importance of regional plate reconstructions for subduction-driven mantle flow models. We suggest that the inclusion of the subduction zones that consumed the South Anuyi Ocean [*Shephard et al*., 2013] account for some features in seismic tomography. While the inclusion of subduction along the Wrangellia Superterrane may account for some high-velocity anomalies in mantle tomography under North America, reasonable mismatch at latitude ~50°N remains. Future work should refine the history of intraoceanic subduction in western Panthalassa.

We show that gradual sinking of predominantly Jurassic circum-Arctic slabs leads to dynamic subsidence (~<1–16 m/Myr) of much of the region from at least 170 Ma until ~70–50 Ma. Importantly, the trend and magnitude of the predicted dynamic topography signal are consistent across a variety of model parameters and absolute reference frames. This illustrates the robustness of our conclusions based on this regionally refined plate reconstruction [*Shephard et al*., 2013]. Maximum rates of subsidence during this period are predicted for the North Slope (<21 m/Myr), the Slave Craton (<15 m/Myr), Banks Island, and Greenland (<12 m/Myr). The best match between the timing and magnitude of our modeled dynamic topography to geological inferences is found at the North Slope and Slave Craton. While largely overlooked in past studies, we suggest that slab-driven vertical motions contribute significantly to observable subsidence and uplift across the region since at least the Cretaceous. Subsequent slowed subsidence or reversal to uplift (typically <1–6 m/Myr) is predicted across the circum-Arctic from ~50 Ma to present day. Siberia and Greenland, as predicted by our models, are exceptions to the region pattern of reversal from long-lived subsidence to uplift and were likely affected by active plume-induced uplift not considered here.

We suggest that subduction-driven dynamic topography contributed to the observed continuous subsidence of the Barents Sea from at least the Late Triassic until ~50 Ma, including Svalbard. A small part of later Cenozoic uplift of many North Atlantic regions might also be explained by dynamic topography, as the region moved over and past the underlying slabs in the mantle. However, additional processes are required to account for the observations, including dynamic uplift associated with a plume, magmatic underplating or uppermost (<350 km) mantle flow. Despite inherent uncertainties, one of the merits of the presented model is to isolate the contribution of subduction-driven dynamic topography from the overall signal of vertical motion. Future advances in such high-resolution plate-mantle models, in seismic tomography, and in quantifying vertical motion from independent geological observations will further constrain plate reconstructions and mantle properties.

Acknowledgments

G.E.S., S.W., M.S., and R.D.M. were supported by Australian Research Council (ARC) grant FL0992245, ARC Linkage grant LP0989312, and ARC Discovery grant DP0987713. G.E.S. was also partly supported by the Research Council of Norway through its Centers of Excellence funding scheme, project 223272. N.F. was supported by Statoil ASA, and M.G. was supported by NSF grant EAR1247022. We would like to thank Bernard Steinberger and an anonymous reviewer for their constructive comments. The associated data for the plate reconstruction of *Shephard et al.* [2013] can be downloaded at ftp://ftp.earthbyte.org/papers/Shephard_etal_Arctic_plate_model and for the *Seton et al.* [2012] model at ftp://ftp.earthbyte.org/papers/Seton_etal_Global_ESR/Seton_etal_Data.zip The global mantle flow models are proprietary; however, selected time-dependent raster images of both the mantle structure and dynamic topography for loading into the plate reconstruction software GPlates (www.gplates.org) can be downloaded from ftp://ftp.earthbyte.org/papers/Shephard_etal_Arctic_Mantle/Shephard_etal_2014.zip.

References

Allen, M. B., and C. E. Davies (2007), Unstable Asia: Active deformation of Siberia revealed by drainage shifts, *Basin Res.*, *19*, 379–392, doi:10.1111/j.1365-2117.2007.00331.x.

Alvey, A., C. Gaina, N. J. Kusznir, and T. H. Torsvik (2008), Integrated crustal thickness mapping and plate reconstructions for the high Arctic, *Earth Planet. Sci. Lett.*, *271*, 310–321.

Anell, I., H. Thybo, and I. M. Artemieva (2009), Cenozoic uplift and subsidence in the North Atlantic region: Geological evidence revisited, *Tectonophysics*, *474*, 78–105.

Artemieva, I. M. (2006), Global 1 × 1 thermal model TC1 for the continental lithosphere: Implications for lithosphere secular evolution, *Tectonophysics*, *416*, 245–277, doi:10.1016/j.tecto.2005.11.022.

Artemieva, I. M., and W. D. Mooney (2001), Thermal thickness and evolution of Precambrian lithosphere: A global study, *J. Geophys. Res.*, *106*, 16,387–16,414, doi:10.1029/2000JB900439.

Backman, J., et al. (2008), Age model and core-seismic integration for the Cenozoic Arctic Coring Expedition sediments from the Lomonosov Ridge, *Paleoceanography*, *23*, PA1S03, doi:10.1029/2007PA001476.

Ballance, P. F. (1993), *In South Pacific Sedimentary Basins*, Sedimentary Basins of the World, vol. 2, edited by P. F. Balance, pp. 93–110, Elsevier, Amsterdam, Netherlands.

Blythe, A. E., J. M. Bird, and G. I. Omar (2010), Deformational history of the central Brooks Range, Alaska: Results from fission-track and 40Ar/39Ar analyses, *Tectonics*, *15*, 440–455, doi:10.1029/95TC03053.

Bower, D. J., M. Gurnis, and M. Seton (2013), Lower mantle structure from paleogeographically constrained dynamic Earth models, *Geochem. Geophys. Geosyst.*, *14*, 44–63, doi:10.1029/2012GC004267.

Boyden, J. A., R. D. Müller, M. Gurnis, T. H. Torsvik, J. A. Clark, M. Turner, H. Ivey-Law, R. J. Watson, and J. S. Cannon (2011), Next-generation plate-tectonic reconstructions using GPlates, in *Geoinformatics: Cyberinfrastructure for the Solid Earth Sciences*, edited by G. R. Keller and C. Baru, pp. 95–114, Cambridge Univ. Press, Cambridge, U. K.

Bunge, H.-P., and S. Grand (2000), Mesozoic plate-motion history below the northeast Pacific Ocean from seismic images of the subducted Farallon slab, *Nature*, *405*, 337–340.

Bunge, H.-P., M. A. Richards, C. Lithgow-Bertelloni, J. R. Baumgardner, S. P. Grand, and B. B. Romanowicz (1998), Time scales and heterogenous structure in geodynamic Earth models, *Science*, *280*, 91–95.

Burke, K., B. Steinberger, T. H. Torsvik, and M. A. Smethurst (2008), Plume generation zones at the margins of large low shear velocity provinces on the core-mantle boundary, *Earth Planet. Sci. Lett.*, *265*, 49–60, doi:10.1016/j.epsl.2007.09.042.

Butterworth, N. P., A. S. Talsma, R. D. Müller, M. Seton, H.-P. Bunge, B. S. A. Schuberth, G. E. Shephard, and C. Heine (2014), Geological, tomographic, kinematic and geodynamic constraints on the dynamics of sinking slabs, *J. Geodyn.*, *73*, 1–13, doi:10.1016/j.jog.2013.10.006.

Cande, S. C., and J. M. Stock (2004), Pacific–Antarctic–Australia motion and the formation of the Macquarie Plate, *Geophys. J. Int.*, *157*, 399–414.

Cande, S. C., J. M. Stock, R. D. Müller, and T. Ishihara (2000), Cenozoic motion between East and West Antarctica, *Nature*, *404*, 145–150.

Clift, P. D., and J. Turner (1998), Paleogene igneous underplating and subsidence anomalies in the Rockall-Faeroe-Shetland area, *Mar. Pet. Geol.*, *15*, 223–243.

Cole, F., K. J. Bird, J. Toro, F. Roure, P. B. O'Sullivan, M. Pawlewicz, and D. G. Howell (1997), An integrated model for the tectonic development of the frontal Brooks Range and Colville Basin 250 km west of the Trans-Alaska Crustal transect, *J. Geophys. Res.*, *102*, 20,685–20,708, doi:10.1029/96JB03670.

Conrad, C. P., and M. D. Behn (2010), Constraints on lithosphere net rotation and asthenospheric viscosity from global mantle flow models and seismic anisotropy, *Geochem. Geophys. Geosyst.*, *11*, Q05W05, doi:10.1029/2009GC002970.

Crosby, A. G., N. White, G. Edwards, and D. J. Shillington (2008), Evolution of the Newfoundland–Iberia conjugate rifted margins, *Earth Planet. Sci. Lett.*, *273*, 214–226.

Davis, E. E., and C. R. B. Lister (1974), Fundamentals of ridge crest topography, *Earth Planet. Sci. Lett.*, *21*, 405–413, doi:10.1016/0012-821X(74)90180-0.

Doré, A. G., E. R. Lundin, L. N. Jensen, Ø. Birkeland, P. E. Eliassen, and C. Fichler (1999), Principal tectonic events in the evolution of the northwest European Atlantic margins, in *Petroleum Geology of Northwest Europe: Proceedings of the 5th Conference*, edited by A. J. Fleet and S. A. R. Boldy, pp. 41–61, Geol. Soc., London, U. K.

Doré, A. G., J. A. Cartwright, M. S. Stoker, J. P. Turner, and N. J. White (2002), Exhumation of the North Atlantic margin: Introduction and background, in *Exhumation of the North Atlantic Margin: Timing, Mechanisms and Implications for Petroleum Exploration*, vol. 196, edited by A. G. Doré et al., *Geol. Soc. Spec. Publ.*, pp. 1–12, Bath, U. K.

Dörr, N., P. D. Clift, F. Lisker, and C. Spiegel (2013), Why is Svalbard an Island? Evidence for two-stage uplift, magmatic underplating and mantle thermal anomalies, *Tectonics*, *32*, 473–486, doi:10.1002/tect.20039.

Fjeldskaar, W., C. Lindholm, J. Dehls, and I. Fjeldskaar (2000), Postglacial uplift, neotectonics and seismicity in Fennoscandia, *Quat. Sci. Rev.*, *19*(14–15), 1413–1422.

Flament, N., M. Gurnis, and R. D. Müller (2013), A review of observations and models of dynamic topography, *Lithosphere*, *5*, 189–210, doi:10.1130/L245.1.

Flament, N., M. Gurnis, S. Williams, M. Seton, J. Skogseid, C. Heine, and R. D. Müller (2014), Topographic asymmetry of the South Atlantic from global models of mantle flow and lithospheric stretching, *Earth Planet. Sci. Lett.*, *387*, 107–119.

Flowers, R. M., A. K. Ault, S. A. Kelley, N. Zhang, and S. Zhong (2012), Epeirogeny or eustasy? Paleozoic-Mesozoic vertical motion of the North American continental interior from thermochronology and implications for mantle dynamics, *Earth Planet. Sci. Lett.*, *317–318*, 436–445.

Gac, S., R. S. Huismans, Y. Y. Podladchikov, and J. I. Faleide (2012), On the origin of the ultradeep East Barents Sea basin, *J. Geophys. Res.*, *117*, B04401, doi:10.1029/2011JB008533.

Gac, S., R. S. Huismans, N. S. C. Simon, Y. Y. Podladchikov, and J. I. Faleide (2013), Formation of intra-cratonic basins by lithospheric shortening and phase changes: A case study from the ultra-deep East Barents Sea basin, *Terra Nova*, *25*, 459–464.

Galushkin, Y., O. Simonenkova, and N. Lopatin (1999), Thermal and maturation modeling of the Urengoy Field, West Siberian Basin: Some special considerations in basin modeling, *AAPG Bull.*, *83*, 1965–1979.

Grand, S. P. (2002), Mantle shear-wave tomography and the fate of subducted slabs, *Philos. Trans. R. Soc. A*, *360*, 2475–2491.

Grand, S. P., R. D. van der Hilst, and S. Widiyantoro (1997), Global seismic tomography: A snapshot of convection in the Earth, *Geol. Soc. Am.*, *7*, 1–7.

Granot, R., S. C. Cande, J. M. Stock, and D. Damaske (2013), Revised Eocene-Oligocene kinematics for the West Antarctic rift system, *Geophys. Res. Lett.*, *40*, 279–284, doi:10.1029/2012GL054181.

Green, P. F., and I. R. Duddy (2010), Synchronous exhumation events around the Arctic including examples from Barents Sea and Alaska North Slope, *Pet. Geol. Conf. Ser.*, *7*, 633–644, doi:10.1144/0070633.

Gurnis, M. (1992), Long-term controls on eustatic and epeirogenic motions by mantle convection, *Geol. Soc. Am.*, *2*, 141–157.

Gurnis, M., and S. Zhong (1991), Generation of long wavelength heterogeneity in the mantle by the dynamic interaction between plates and convection, *Geophys. Res. Lett.*, *18*, 581–584, doi:10.1029/91GL00823.

Gurnis, M., M. Turner, S. Zahirovic, L. DiCaprio, S. Spasojevic, R. Müller, J. Boyden, M. Seton, V. Manea, and D. Bower (2012), Plate tectonic reconstructions with continuously closing plates, *Comput. Geosci.*, *38*, 35–42.

Hager, B. H., R. W. Clayton, M. A. Richards, R. P. Comer, and A. M. Dziewonski (1985), Lower mantle heterogeneity, dynamic topography and the geoid, *Nature*, *313*(6003), 541–545, doi:10.1038/313541a0.

Holt, P. J., J. van Hunen, and M. B. Allen (2012), Subsidence of the West Siberian Basin: Effects of a mantle plume impact, *Geology*, *40*, 703–706.

Husson, L. (2006), Dynamic topography above retreating subduction zones, *Geology*, *34*, 741–744, doi:10.1130/G22436.1.

Japsen, P., and J. A. Chalmers (2000), Neogene uplift and tectonics around the North Atlantic: Overview, *Global Planet. Change*, *24*, 165–173.

Lekic, V., S. Cottaar, A. Dziewonski, and B. Romanowicz (2012), Cluster analysis of global lower mantle tomography: A new class of structure and implications for chemical heterogeneity, *Earth Planet. Sci. Lett.*, *357–358*, 68–77, doi:10.1016/j.epsl.2012.09.014.

Lithgow-Bertelloni, C., and P. G. Silver (1998), Dynamic topography, plate driving forces and the African superswell, *Nature*, *395*, 269–272, doi:10.1038/26212.

Liu, L., S. Spasojević, and M. Gurnis (2008), Reconstructing Farallon plate subduction beneath North America back to the Late Cretaceous, *Science*, *322*, 934–938, doi:10.1126/science.1162921.

Liu, L., G. E. Shephard, M. Gurnis, and R. D. Müller (2009), Modelling Arctic subduction dynamics, Geological Society of America (GSA), Penrose Conference, Tectonic development of the Amerasia Basin, Banff, 4–9th Oct.

Lundin, E. R., and A. G. Doré (1997), A tectonic model for the Norwegian passive margin with implications for the NE Atlantic; Early Cretaceous to break-up, *J. Geol. Soc. London*, *154*, 545–550.
McNamara, A. K., and S. Zhong (2005), Thermochemical structures beneath Africa and the Pacific Ocean, *Nature*, *437*, 1136–1139, doi:10.1038/nature04066.
Minakov, A. N., and Y. Y. Podladchikov (2012), Tectonic subsidence of the Lomonosov Ridge, *Geology*, *40*, 99–102, doi:10.1130/G32445.1.
Moran, K., et al. (2006), The Cenozoic palaeoenvironment of the Arctic Ocean, *Nature*, *441*, 601–605, doi:10.1038/nature04800.
Nokleberg, W. J., L. M. Parfenov, J. W. H. Monger, I. O. Norton, A. I. Khanchuk, D. B. Stone, C. R. Scotese, D. W. Scholl, and K. Fujita (2000), *Phanerozoic Tectonic Evolution of the Circum-North Pacific*, Professional Paper, vol. 1626, 122 pp., U.S. Geol. Surv, Washington, D. C.
O'Neill, C., R. D. Müller, and B. Steinberger (2005), On the uncertainties in hotspot reconstructions, and the significance of moving hotspot reference frames, *Geochem. Geophys. Geosyst.*, *6*, Q04003, doi:10.1029/2004GC000784.
Poag, C. W., and W. D. Sevon (1989), A record of appalachian denudation in postdrift Mesozoic and Cenozoic sedimentary deposits of the U.S. Middle Atlantic continental margin, *Geomorphology*, *2*, 19–157.
Pysklywec, R. N., and J. X. Mitrovica (1998), Mantle flow mechanisms for the large-scale subsidence of continental interiors, *Geology*, *26*, 687–690.
Ritsema, J., A. Deuss, H. J. van Heijsy, and J. H. Woodhouse (2010), S40RTS: A degree-40 shear-velocity model for the mantle from new Rayleigh wave dispersion, teleseismic traveltime and normal-mode splitting function measurements, *Geophys. J. Int.*, *184*, 1223–1236, doi:10.1111/j.1365-246X.2010.04884.x.
Saunders, A. D., R. W. England, M. K. Reichow, and R. V. White (2005), A mantle plume origin for the Siberian traps: Uplift and extension in the West Siberian Basin, Russia, *Lithos*, *79*, 407–424, doi:10.1016/j.lithos.2004.09.010.
Scheck-Wenderoth, M., T. Raum, J. I. Faleide, R. Mjelde, and B. Horsfield (2007), The transition from the continent to the ocean: A deeper view of the Norwegian margin, *J. Geol. Soc.*, *164*, 855–868.
Seton, M., et al. (2012), Global continental and ocean basin reconstructions since 200 Ma, *Earth Sci. Rev.*, *113*, 212–270, doi:10.1016/j.earscirev.2012.03.002.
Shephard, G. E., R. D. Müller, L. Liu, and M. Gurnis (2010), Miocene drainage reversal of the Amazon River driven by plate-mantle interaction, *Nat. Geosci.*, *3*, 870–875, doi:10.1038/ngeo1017.
Shephard, G. E., H. P. Bunge, B. S. A. Schuberth, R. D. Müller, A. S. Talsma, C. Moder, and T. C. W. Landgrebe (2012), Testing absolute plate reference frames and the implications for the generation of geodynamic mantle heterogeneity structure, *Earth Planet. Sci. Lett.*, *317–318*, 204–217.
Shephard, G. E., R. D. Müller, and M. Seton (2013), The tectonic evolution of the Arctic since Pangea breakup: Integrating constraints from surface geology and geophysics with mantle structure, *Earth Sci. Rev.*, *124*, 148–183.
Sigloch, K. (2011), Mantle provinces under North America from multifrequency P wave tomography, *Geochem. Geophys. Geosyst.*, *12*, Q02W08, doi:10.1029/2010GC003421.
Sigloch, K., and M. Mihalynuk (2013), Intra-oceanic subduction shaped the assembly of Cordilleran North America, *Nature*, *496*, 50–56, doi:10.1038/nature12019.
Simmons, N. A., A. M. Forte, L. Boschi, and S. P. Grand (2010), GyPSuM: A joint tomographic model of mantle density and seismic wave speeds, *J. Geophys. Res.*, *115*, B12310, doi:10.1029/2010JB007631.
Skogseid, J., T. Pedersen, and V. B. Larsen (1992), Vøring Basin: Subsidence and tectonic evolution, *Norw. Pet. Soc. Spec. Publ.*, *1*, 55–82.
Spasojevic, S., and M. Gurnis (2012), Sea level and vertical motion of continents from dynamic Earth models since the Late Cretaceous, *Am. Assoc. Pet. Geol. Bull.*, *96*(11), 2037–2064.
Spasojevic, S., L. Liu, M. Gurnis, and R. D. Müller (2008), The case for dynamic subsidence of the U.S. east coast since the Eocene, *Geophys. Res. Lett.*, *35*, L08305, doi:10.1029/2008GL033511.
Spasojevic, S., L. Liu, and M. Gurnis (2009), Adjoint models of mantle convection with seismic, plate motion, and stratigraphic constraints: North America since the Late Cretaceous, *Geochem. Geophys. Geosyst.*, *10*, Q05W02, doi:10.1029/2008GC002345.
Steinberger, B., and T. Torsvik (2008), Absolute plate motions and true polar wander in the absence of hotspot tracks, *Nature*, *452*, 620–623, doi:10.1038/nature06824.
Stuevold, L. M., and O. Eldholm (1996), Cenozoic uplift of Fennoscandia inferred from a study of the mid-Norwegian margin, *Global Planet. Change*, *12*, 359–386.
Stuevold, L. M., J. Skogseid, and O. Eldholm (1992), Post-Cretaceous uplift events on the Vøring continental margin, *Geology*, *20*, 919–922.
Sutherland, R. (1995), The Australia-Pacific boundary and Cenozoic plate motions in the SW Pacific: Some constraints from Geosat data, *Tectonics*, *14*, 819–831, doi:10.1029/95TC00930.
Torsvik, T., R. D. Müller, R. van der Voo, B. Steinberger, and C. Gaina (2008), Global plate motion frames: Toward a unified model, *Rev. Geophys.*, *46*, RG3004, doi:10.1029/2007RG000227.
Trop, J. M., K. D. Ridgway, J. D. Manuszak, and P. Layer (2002), Mesozoic sedimentary-basin development on the allochthonous Wrangellia composite terrane, Wrangell Mountains basin Alaska: A long-term record of terrane migration and arc construction, *Geol Soc. Am. Bull.*, *114*, 693–717.
Vågnes, E., J. I. Faleide, and S. T. Gudlaugsson (1992), Glacial erosion and tectonic uplift in the Barents Sea, *Nor. Geol. Tidsskr.*, *72*, 333–338.
Van der Meer, D. G., W. Spakman, D. J. J. van Hinsbergen, M. L. Amaru, and T. H. Torsvik (2010), Towards absolute plate motions constrained by lower-mantle slab remnants, *Nat. Geosci.*, *3*, 36–40, doi:10.1038/NGEO708.
Van der Voo, R., W. Spakman, and H. Bijwaard (1999), Tethyan subducted slabs under India, *Earth Planet. Sci. Lett.*, *171*, 7–20.
Vyssotski, A. V., V. N. Vyssotski, and A. A. Nezhdanov (2006), Evolution of the West Siberian Basin, *Mar. Pet. Geol.*, *23*, 93–126, doi:10.1016/j.marpetgeo.2005.03.002.
Wheeler, P., and N. White (2000), Quest for dynamic topography: Observations from Southeast Asia, *Geology*, *28*, 963–966, doi:10.1130/0091-7613(2000)28<963:QFDTOF>2.0.CO;2.
Wilson, F. H., R. L. Detterman, and G. D. DuBois (1999), Digital data for geologic framework of the Alaska Peninsula, Southwest Alaska and the Alaska Peninsula Terrane, *USGS Open-File Rep., 99-317*.
Zahirovic, S., M. Seton, and R. D. Müller (2013), The Cretaceous and Cenozoic tectonic evolution of Southeast Asia, *Solid Earth Discuss.*, *5*, 1335–1422, doi:10.5194/sed-5-1335-2013.
Zhang, N., S. Zhong, and R. M. Flowers (2012), Predicting and testing continental vertical motion histories since the Paleozoic, *Earth Planet. Sci. Lett.*, *317-318*, 426–435, doi:10.1016/j.epsl.2011.10.041.
Zhong, S., M. Zuber, L. N. Moresi, and M. Gurnis (2000), Role of temperature-dependent viscosity and surface plates in spherical shell models of mantle convection, *J. Geophys. Res.*, *105*, 11,063–11,082, doi:10.1029/2000JB900003.